Gaussian Beam Summation for Diffraction in Inhomogeneous Media Based on the Grid Based Particle Method

Shingyu Leung[1,*], and Hongkai Zhao[2]

[1] *Department of Mathematics, Hong Kong University of Science and Technology, Clear Water Bay, Hong Kong.*
[2] *Department of Mathematics, University of California at Irvine, Irvine, CA 92697-3875, USA.*

Abstract. We develop an efficient numerical method to compute single slit or double slit diffraction patterns from high frequency wave in inhomogeneous media. We approximate the high frequency asymptotic solution to the Helmholtz equation using the Eulerian Gaussian beam summation proposed in [21, 20]. The emitted rays from a slit are embedded in the phase space using an *open* segment. The evolution of this open curve is accurately computed using the recently developed Grid Based Particle Method [24] which results in a very efficient computational algorithm. Following the grid based particle method we proposed in [24, 23], we represent the open curve or the open surface by meshless Lagrangian particles sampled according to an underlying fixed Eulerian mesh. The end-points of the open curve are tracked explicitly and consistently with interior particles. To construct the overall wavefield, each of these sampling particles also carry necessary quantities that are obtained by solving advection-reaction equations. Numerical experiments show that the resulting method can model diffraction patterns in inhomogeneous media accurately, even in the occurrence of caustics.

1 Introduction

Diffraction is one of the most commonly seen phenomena in wave propagation. Whenever an incident wave encounters an obstacle, it bends itself around such a small obstacle or it spreads itself out through small openings. In this paper, we concentrate on the second case and we will consider the single slit diffraction or the double slit diffraction. The setup of the problem is shown in figure 1. In both of these experiments, we for simplicity consider only that the incident wave has a plane wavefront when it hits the slit(s). This can be done by, for example, assuming that a point source is placed far away from the

*Corresponding author. *Email addresses:* masyleung@ust.hk (S. Leung), zhao@math.uci.edu (H. Zhao)

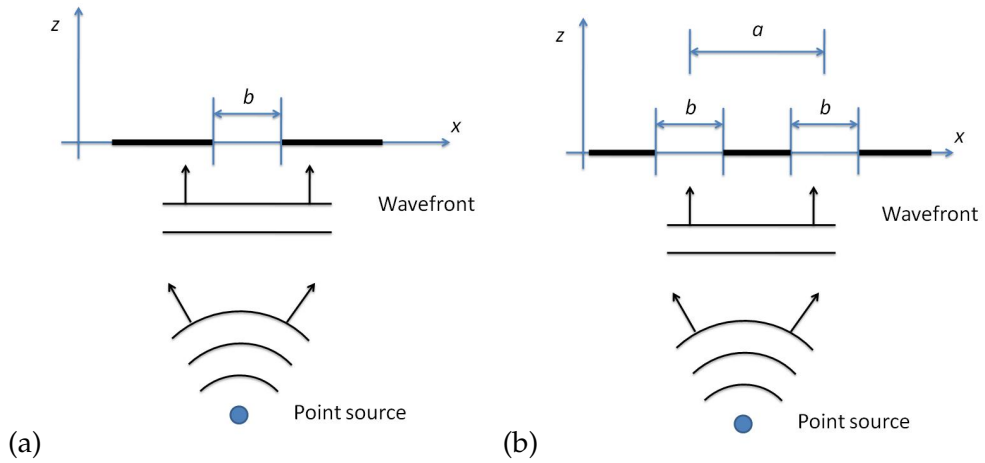

Figure 1: Setup for (a) single slit diffraction and (b) double dlit diffraction.

slit(s). We let b be the width of a slit. In double slit diffraction, we further let a be the distance between two slits. The incident wave has an incident wavelength $2\pi/\omega \ll b$.

Mathematically, such behavior cannot be predicted by solving the wave equation using the usual geometrical optics method. This high frequency asymptotic method computes wavefield only along ray trajectories which are governed by the Fremat's principle. In shadow region where no ray is reaching, the method fails to explain for the spreading of diffraction wave. There is no mechanism in usual geometrical optics to explain for the bending of ray near an obstacle.

Various methods were proposed to include the diffraction phenomenon in the high frequency asymptotic solution. One of the first attempts was the geometrical theory of diffraction (GTD) [33, 32, 17, 26]. The idea was to introduce diffracted rays in addition to the typical geometrical optics rays. These extra rays added correction to the asymptotic expansion by geometrical optics. Different types of diffracted rays were introduced to account for various kinds of scatterer surfaces [25]. However, similar to geometrical optics, typical GTD fails near caustics and special treatment has to be introduced to extend the usual GTD to compute the wavefield near these transition regions [18]. Another approach was the (ray-based) complex geometrical optics (CGO) which dealt with complex rays instead of usual real rays as in the original geometrical optics [9, 10, 11]. Diffraction of an initial beam of the Gaussian form was correctly calculated even in some inhomogeneous media [10, 4, 19, 3]. Relating to the CGO, the Gaussian beam summation method can also provide a powerful framework for constructing uniform asymptotic solutions systematically even at caustics. The idea underlying Gaussian beams is simply to build asymptotic solutions to partial differential equations concentrated on a single curve through the domain; this single curve is nothing but a ray as shown in [31]. The existence of such solutions has been known to the pure mathematics community since sometime

in the 1960s [1], and these solutions have been used to obtain results on propagation of singularities in hyperbolic PDEs [16, 31]. An integral superposition of these solutions can be used to define a more general solution that is not necessarily concentrated on a single curve. Gaussian beams can also be used to treat pseudo-differential equations in a natural way, including the Helmholtz equation and the Schrödinger equation.

In geophysical applications, Gaussian beam superpositions have been used for seismic wave modeling [7] and for seismic wave migration [15]. The numerical implementations in these works were based on ray-centered coordinates which proved to be computationally inefficient. More recently, based on [31, 40], we proposed a purely Eulerian computational approach in [21] and [20] which overcomes some of these difficulties. The idea is to first follow the ansatz proposed in [31, 40] to construct Gaussian beams to the Helmholtz equation along central rays. Mathematically, this ansatz constructs an approximate phase function with an imaginary part as a Taylor expansion around a central ray by using phase derivatives on the central ray. To have a corresponding Eulerian formulation capturing multi-valued phases and caustics, [21, 20] have applied the Eulerian Gaussian beam approach. The Eulerian method proposed in [21, 20] is based on level sets and paraxial Liouville equations [29, 22, 30] and is designed to solve Helmholtz equations in the high frequency regime.

In this paper, we will apply the Gaussian beam summation method to compute diffraction patterns in both homogeneous and inhomogeneous media. Even though we are limiting our discussion to only the single slit and the double slit diffraction, the proposed algorithm can be naturally applied to diffraction patterns due to multiple slits (of any apertures and locations). One main idea in this paper is to implicitly represent *all* beams coming out from a slit in the phase space using an *open curve*. This open segment will be moved according to the characteristics of an Liouville equation.

In this work, we will apply the method we have recently introduced in [24, 23] which can naturally model various motions of an open curve or an open surface in two dimensions and three dimensions. When we are constructing the wavefield, we also need to solve Liouville equations along with the interface motion. We will extend the approach in [24] to solve advection-reaction equations. The approach is to first solve the reaction part along the characteristic using high order ODE solver at each time step and then to approximate the quantity using least square fitting at the new sampling locations.

The advantages of this approach are multi-folded. Just like the Eulerian methods we developed in [21, 20], the framework in this paper gives a quasi-uniform resolution of ray distribution so that the resulting Gaussian beam summation will as well have a uniform resolution. On the other hand, unlike the Eulerian Gaussian beam approaches based on the level set method, the current formulation does not require interpolation of various quantities on the underlying mesh in order to construct the overall wavefield. Moreover, the ability to accurately deal with the motion of an open curve and surfaces with high co-dimensionality makes the proposed algorithm computationally accurate and efficient.

The rest of the paper will be organized as follows. We will first describe in Section 2 the construction of the high frequency asymptotic solution to the paraxial wave equation

using the Eulerian Gaussian beams summations. In Section 3, we will introduce a new numerical method for solving the necessary partial differential equations for the summation process. Various examples will be given in Section 4 to demonstrate diffractions of the wave equation in different apertures and media.

2 Gaussian Beams (GB)

2.1 Construction of Lagrangian Gaussian beams

We construct an asymptotically valid solution $\Psi(x,z;\omega)$ for the Helmholtz wave equation concentrated on a single curve γ. Namely, $|\Psi(x,z;\omega)|$ is small away from γ, and it will satisfy the Helmholtz equation up to $O(\omega^{-M})$ for some fixed positive number M under some appropriate norm [31, 39]. Here we are interested in constructing the lowest-order Gaussian beam so that the Helmholtz equation will be satisfied up to $O(\omega^{-1/2})$ in the L^2 sense.

To construct such Gaussian beams for the Helmholtz equation,

$$\nabla^2 U + \frac{\omega^2}{c^2(x,z)} U = 0,\ x \in \Omega \subset \mathbb{R}^2 \tag{2.1}$$

we follow [31, 21, 40, 20] and start with the WKBJ ansatz,

$$U(x,z) \approx A(x,z) \exp(i\omega\tau(x,z)). \tag{2.2}$$

The functions $A(x,z)$ and $\tau(x,z)$ are both assumed to be smooth, and these requirements are feasible because the beam solution is constructed to be concentrated on a single curve; this is the essential difference between traditional WKBJ asymptotic solutions and Gaussian beam solutions. As a result, the requirements on the phase function τ are slightly different from those of traditional WKBJ asymptotics. We will require that τ is real valued on γ, but away from this curve γ, τ can be complex valued with the restriction that the imaginary part of the second-order derivative τ_{xx} is positive definite.

Substituting this ansatz into (2.1) and equating the terms of leading order, we obtain the eikonal equation for the traveltime τ and the transport equation for the amplitude A,

$$\begin{aligned} |\nabla\tau|^2 &= \frac{1}{c^2} \\ \nabla\tau\cdot\nabla A + \frac{1}{2} A\nabla^2\tau &= 0. \end{aligned} \tag{2.3}$$

In many applications, let z be vertically up, we will assume that the wave will travel only in the positive z-direction and therefore the traveltime field satisfies

$$\frac{\partial\tau}{\partial z} > 0, \tag{2.4}$$

i.e. rays are subhorizontal. In this case, we introduce the following Hamiltonian for the Helmholtz equation,

$$H(x,p) = -\sqrt{\frac{1}{c^2(x,z)} - p^2}, \tag{2.5}$$

where $p = \tau_x$.

According to the Gaussian beam theory [31], the ray γ is nothing but the x-projection of bicharacteristics $(x(z),\theta(z))$ satisfying the following Hamiltonian system,

$$\begin{aligned} \dot{x} &= \frac{dx}{dz} = \tan\theta \\ \dot{\theta} &= \frac{d\theta}{dz} = \frac{1}{c}(c_z \tan\theta - c_x), \end{aligned} \tag{2.6}$$

where θ is the angle between the ray direction and the positive z-axis and the phase variable p relates to this ray angle through the relationship $p = \sin\theta / c(x,z)$. Along bicharacteristics, the phase function satisfies

$$\dot{\tau} = \frac{d\tau}{dz} = \frac{1}{c\cos\theta}. \tag{2.7}$$

To determine the second order derivative τ_{xx} along bicharacteristics, we solve the following variational system for matrix-valued solutions $B(z)$ and $C(z)$:

$$\begin{aligned} \dot{B} &= -H_{xp}^T B - H_{xx} C,\ B|_{z=0} = B_0, \\ \dot{C} &= H_{pp} B + H_{xp} C,\ C|_{z=0} = C_0, \end{aligned} \tag{2.8}$$

where the derivative is the material derivative along the characteristics, I is the identity matrix, the matrix B_0 is chosen to take into account the initial phase function and to have an imaginary part which is positive definite. In two dimension, we have

$$\begin{aligned} H_{xx} &= \frac{\cos^2\theta(cc_{xx} - 3c_x^2) + c_x^2}{c^3\cos^3\theta} \\ H_{xp} &= \frac{c_x \tan\theta}{c\cos^2\theta} \\ H_{pp} &= \frac{c}{\cos^3\theta}. \end{aligned} \tag{2.9}$$

Here $B = B(z;x_0,\theta_0)$ and $C = C(z;x_0,\theta_0)$ are taken to be the variations of $p = p(z;x_0,\theta_0)$ and $x = x(z;x_0,\theta_0)$ along the bi-characteristics with respect to the initial point $x_0 = \alpha$,

$$B(z;x_0,\theta_0) = \frac{\partial p}{\partial \alpha},\ C(z;x_0,\theta_0) = \frac{\partial x}{\partial \alpha}. \tag{2.10}$$

We notice that BC^{-1} yields the Hessian of the phase function τ along the bi-characteristics. Solution to the above equations exists on any interval $t \in [0,T]$. Moreover, we have the following lemma on the bound of the solution [31, 40]

Lemma 2.1. Under the above assumptions, $C(z)$ is non-singular for any z, and $\mathrm{Im}(BC^{-1})$ is positive definite.

Since $p(z)=\tau_x(z)$ along bicharacteristics, we can use the following second-order Taylor expansion to define a smooth global approximate phase function:

$$\begin{aligned}\tau(x,z;x_0,\theta_0) &= \tau(z;x_0,\theta_0)+p(z;x_0,\theta_0)\cdot(x-x(z;x_0,\theta_0))\\ &\quad+\frac{1}{2}(x-x(z;x_0,\theta_0))^T(BC^{-1})(x-x(z;x_0,\theta_0)).\end{aligned} \tag{2.11}$$

Next we need to determine the amplitude function A. According to the beam theory, the amplitude function A satisfies the transport equation

$$\dot{\mathcal{A}}=-\frac{1}{2}\mathrm{trace}(BC^{-1})\,\mathcal{A},\ \mathcal{A}|_{z=0}=\mathcal{A}_0(x_0,\theta_0), \tag{2.12}$$

with $\mathcal{A}=A\sqrt{\cos\theta/c}$. To reduce the number of equations, we introduce $M=BC^{-1}$ and simplify equations (2.8) and (2.12) to the following Ricatti equation

$$\begin{aligned}\dot{M} &= -(H_{xx}+2H_{xp}M+H_{pp}M^2)\\ \dot{\mathcal{A}} &= -\frac{1}{2}\mathrm{tr}(M)\mathcal{A}.\end{aligned} \tag{2.13}$$

Numerically, it is hard to guarantee the condition in Lemma 2.1 by solving the equation of M using typical integrators such as TVD-RK3. Accumulation of numerical error could drive the imaginary part of M to be negative and therefore the magnitude of the beam solution will blow up as $|x-x(z;x_0,\theta_0)|\to\infty$. To better impose the positivity of $\mathrm{Im}(BC^{-1})$ in Lemma 2.1, we modify the imaginary part of $M=M_r+iM_i$ by introducing $\mathcal{M}=M_r+i\mathcal{M}_i$ and $\mathcal{M}_i=\log M_i$ so that (2.13) becomes

$$\begin{aligned}\dot{M}_r &= -[H_{xx}+2H_{xp}M_r+H_{pp}(M_r^2-\exp(2\mathcal{M}_i))]\\ \dot{\mathcal{M}}_i &= -2(H_{xp}+H_{pp}M_r)\\ \dot{\mathcal{A}} &= -\frac{1}{2}[M_r+i\exp(\mathcal{M}_i)]\mathcal{A}.\end{aligned} \tag{2.14}$$

To obtain a smooth global approximate amplitude function, we simply use the extension

$$\mathcal{A}(x,z;x_0,\theta_0)=\mathcal{A}(z;x_0,\theta_0). \tag{2.15}$$

It is possible to construct a higher order approximation to the amplitude function [39]. However, without taking into account of a higher order Taylors approximation of the phase function, such a high order approximation will not result in a high order construction of the overall wavefield. In practice, we can obtain good asymptotic solution already using only the zeroth-order approximation to the amplitude function with a second-order Taylor approximation to the phase function.

Inserting (2.11) and (2.15) into the WKBJ ansatz yields an asymptotically valid solution

$$\Psi(x,z;x_0,\theta_0) = A(x,z;x_0,\theta_0)\exp[i\omega\tau(x,z;x_0,\theta_0)] \tag{2.16}$$

concentrated on a single smooth curve γ which is the x-projection of the bicharacteristic emanating from (x_0,θ_0) at $z=z_0=0$.

The asymptotic solution of the overall wavefield is obtained by integrating all the beams parametrized by the initial point (x_0,θ_0),

$$U(x,z) = d(\epsilon,\omega,n)\int_{\theta_0}\int_{x_0}\Psi(x,z;x_0,\theta_0)dx_0d\theta_0, \tag{2.17}$$

for some normalization constant $d(\epsilon,\omega,n)$.

2.2 Initializing Gaussian beams

If $A_0(x)$ and $\tilde{\tau}_0(x)$ are given in specific expressions, then we may use the following strategy to initialize beam propagation:

$$\begin{aligned}
x|_{z=0} &= x_0 \\
\theta|_{z=0} &= \theta_0 = \sin^{-1}\left[c(x_0,0)\frac{\partial\tilde{\tau}_0}{\partial x}(x_0)\right] \\
\tau|_{z=0} &= \tilde{\tau}_0(x_0) \\
M|_{z=0} &= M_0 = \frac{\partial^2\tilde{\tau}_0}{\partial x^2}(x_0)\cos\theta_0 + i\epsilon\cos^2\theta_0 \\
\mathcal{A}|_{z=0} &= \mathcal{A}_0(x_0).
\end{aligned} \tag{2.18}$$

Consequently, the resulting beam ingredients are functions of x_0 only, and the approximate functions $\tau(x,z;x_0,\theta_0)=\tau(x,z;x_0)$ and $\mathcal{A}(x,z;x_0,\theta_0)=\mathcal{A}(x,z;x_0)$. Furthermore, the beam summation formula will be modified to be the following:

$$U(x,z) = d(\epsilon,\omega,n)\int_{x_0}\Psi(x,z;x_0)dx_0, \tag{2.19}$$

where

$$\begin{aligned}
\Psi(x,z;x_0) &= A(x,z;x_0)\exp[i\omega\tau(x,z;x_0)], \\
A(x,z;x_0) &= A(z;x_0), \\
\tau(x,z;x_0) &= \tau(z;x_0) + p(z;x_0)\cdot[x-x(z;x_0)] + \\
&\quad \frac{1}{2}[x-x(z;x_0)]^T M[x-x(z;x_0)].
\end{aligned} \tag{2.20}$$

The following lemma proved in [39] holds in terms of recovering the initial data by the initial beam summation:

Lemma 2.2. Let $\phi_0 \in C^\infty(\mathbb{R}^n)$ be a real-valued function and $a_0 \in C_0^\infty(\mathbb{R}^n)$. Define

$$\begin{aligned} u(x) &= a_0(x)\exp[i\omega\phi_0(x)] \\ v(x;y) &= \left(\frac{\epsilon\omega}{2\pi}\right)^{\frac{n}{2}} a_0(y) \\ &\quad \exp\left\{i\omega\left[\phi_0(y)+\phi_0'(y)(x-y)\right]+\frac{\omega}{2}[i\phi_0''(y)-\epsilon](x-y)^2\right\}. \end{aligned} \tag{2.21}$$

Then

$$\left|\left|u(x)-\int_{\mathbb{R}^n} v(x;y)dy\right|\right|_{L^2} \leq C\left(\frac{1}{\epsilon\omega}\right)^{1/2} \tag{2.22}$$

for some constant C.

The parameter ϵ in the beam decomposition controls the initial beam width since the amplitude of the beam decays away from the center in the order of

$$O\left(\exp\left[\frac{-\epsilon\omega}{2}(x-y)^2\right]\right). \tag{2.23}$$

Theoretically, this parameter will not affect the asymptotic order as $\omega \to \infty$ if it is independent of ω and therefore we can arbitrarily pick this width. One simple way is to pick unity for ϵ. In this case, as seen from the estimate, the initial condition of this particular asymptotic decomposition converges to the exact initial profile in the order of $O(\omega^{-1/2})$.

In numerical implementation, on the other hand, numerical quadrature for the beam integral will introduce errors as well. Suppose that we shoot out rays parameterized by y with a uniform spacing Δx, and we approximate the integral by a simple midpoint quadrature. Then the overall error in approximating the initial wavefield will be $O\left((\epsilon\omega)^{-1/2}+\Delta x^2\right)$. If $\epsilon=1$, then the error is $O\left(\omega^{-1/2}+\Delta x^2\right)$; in other words, if ω is fixed and we increase the number of beams by letting $\Delta x \to 0$, then the approximation error in the initial wavefield is still in the order of $\omega^{-1/2}$, which is undesirable.

In [20], we have proposed to choose the initial beam width ϵ according to ω and Δx so that the error in the decomposition is $O(\Delta x)$ which converges to zero as we increase the number of beams. Consider one Gaussian centered at zero in the form of $\exp(-\epsilon\omega y^2/2)$, which has the standard deviation of $\sigma = 1/\sqrt{\epsilon\omega}$. Since this Gaussian decays to almost zero 3σ away from the center, we have proposed to resolve this Gaussian using a fixed number of grid points. Numerically, we use three grid points to resolve 3σ, which gives $\epsilon = 1/\omega\Delta x^2$.

This particular choice of ϵ, however, depends explicitly on ω. This might affect the asymptotic order as $\omega \to \infty$. To simplify the analysis in the order of convergence of the asymptotic solution, we take $\Delta x = O(\omega^{-1/2})$ which gives $\epsilon = 1/\omega\Delta x^2 = O(1)$. So the typical Gaussian beam theory [31, 40] (which uses $\epsilon = 1$) follows which gives the asymptotic solution of order $O(\omega^{-1/2})$.

Other type of initial beam decomposition is possible. In [20], we have proposed and have systematically studied various way to initialize each Gaussian beams components. We refer interested reader to that paper for a more detailed description.

2.3 Eulerian Gaussian Beams (EGB)

By the level set methodology we embed the ray tracing system into the Liouville equation in phase space. Let $\phi(x,\theta,z)\in\mathbb{R}$, $\psi(x,\theta,z)\in\mathbb{R}$, and $T(x,\theta,z)\in\mathbb{R}$. We have the following level set equations and the phase equation,

$$\begin{aligned}
\phi_z+u\cdot\phi_x+v\cdot\phi_\theta &= 0,\ \phi(x,\theta,0)=x,\\
\psi_z+u\cdot\psi_x+v\cdot\psi_\theta &= 0,\ \psi(x,\theta,0)=\theta,\\
T_z+u\cdot T_x+v\cdot T_\theta &= \frac{1}{c\cos\theta},\ T(x,\theta,0)=\tau_0(x),
\end{aligned}\tag{2.24}$$

where $u=\dot{x}$ and $v=\dot{\theta}$. Similarly we have the equations for A and M,

$$\begin{aligned}
\mathcal{A}_z+u\cdot\mathcal{A}_x+v\cdot\mathcal{A}_\theta &= -\frac{1}{2}M\mathcal{A},\\
M_z+u\cdot M_x+v\cdot M_\theta &= -(H_{xx}+2H_{xp}M+H_{pp}M^2),
\end{aligned}\tag{2.25}$$

with the initial conditions

$$\begin{aligned}
\mathcal{A}|_{z=0} &= \mathcal{A}_0(x,\theta),\\
M|_{z=0} &= M_0(x,\theta).
\end{aligned}\tag{2.26}$$

In the previous subsection, we have described the way to initialize the beam in the Lagrangian framework. Here, on the other hand, the function A and M are defined in the whole phase space even though all necessary components to construct the wavefield are required on the level set

$$\Gamma_0=\{\sin(\psi)/c(\phi,0)-\tilde{\tau}_0'(\phi)=0\}.\tag{2.27}$$

There is no unique way how to embed the initial condition for A and M and extend them from the level set Γ_0 to the entire phase space. One simple possibility is to set $A_0(x,\theta)=A_0(x)$ and $M_0(x,\theta)=\frac{\partial^2\tilde{\tau}_0}{\partial x^2}(x)\cos\theta+i\epsilon\cos^2\theta$. Another way is to extend the quantities orthogonally away from the zero level set as in the usual level set method [41, 27].

Now we have all ingredients for constructing Eulerian Gaussian beams solution for $z>0$. The first step is to extract the necessary information by looking into the zero level set defined by

$$\Gamma(z)=\left\{(x,\theta):\frac{\sin(\psi(x,\theta,z))}{c}-\frac{\partial\tilde{\tau}_0[\phi(x,\theta,z)]}{\partial x}=0\right\}.\tag{2.28}$$

Then the wavefield can be computed by

$$\begin{aligned}
U(x,z) &= d(\epsilon,\omega,n)\int_{x',\theta'}\Psi(x,z;x',\theta')\delta[\Gamma(z)]dx'd\theta'\\
&= d(\epsilon,\omega,n)\int_{\Gamma(0)}\Psi(x,z;x',\theta'(x'))dx',
\end{aligned}\tag{2.29}$$

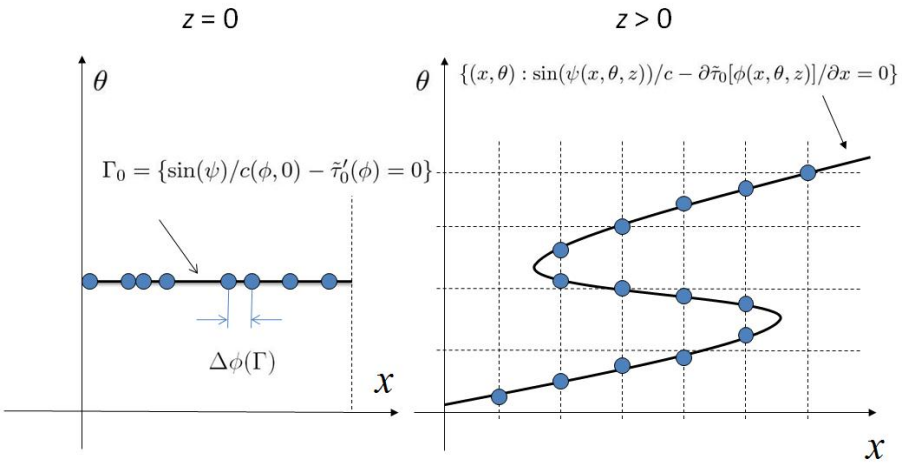

Figure 2: Eulerian Gaussian Beam with the initial wavefunction decomposed using the asymptotic decomposition. The set of sampling points Γ in [21, 20] are shown in blue dots. The useful level set is plotted using a black solid line.

Numerically, however, the implementation of the δ-function could be tricky. One has to smooth it across several grid size and to replace it by a discrete $\delta_{\Delta x}$-function. Another approach described in [21, 20] is to first explicitly determine the set of points on the zero level set which intersect with the grid lines. Then one interpolates all necessary components at these locations and then integrates them to get the wavefunction, as shown in figure 2. We refer interested readers to those references for further explanations on this approach.

In the next section, we will describe a new grid-based particle method which does not require any extension from the necessary level set to the whole computational domain and also does not need any extraction of the $\Gamma(z)$ level set in the summation process. We will further address this issue in Section 2.4.

2.4 Eulerian Gaussian Beams for Single/Double Slit Diffraction

2.4.1 Representation Using Open Curves

Up to this point, we have introduced the Eulerian Gaussian beams approach to construct the high frequency asymptotic solution to the Helmholtz equation. However, the above construction requires that the initial wavefield is given for all $x \in \mathbb{R}$. This is numerically very inefficient. Since the solution to the transport equation (2.12) is

$$A(z) = \frac{A_0(x_0,\theta_0)}{\sqrt{\det(C(z;x_0,\theta_0))}}, \tag{2.30}$$

all beams with $A_0 = 0$ contributes nothing to the overall wavefield for any z. More importantly, when we are modeling the diffraction from a slit, the initial wavefield is defined only for $x \in \Omega_{\text{slit}} \subset \mathbb{R}$, where Ω_{slit} is the slit locations. For example, in the single slit diffraction as shown in figure 1, the initial wavefield is defined for the b-width region. In the Eulerian formulation, this implies that we are given and are interested only on one segment (single slit) or several segments (multiple slits) of the level set in the phase space given by

$$\Gamma_{\text{slit}}(z) = \left\{ (x,\theta) : \frac{\sin(\psi(x,\theta,z))}{c(x,z)} - \frac{\partial \tilde{\tau}_0[\phi(x,\theta,z)]}{\partial x} = 0 \text{ and } \phi(x,\theta,z) \in \Omega_{\text{slit}} \right\}. \tag{2.31}$$

The summation formula to construct the wavefield can be further simplified to

$$\begin{aligned} U(x,z) &= d(\epsilon,\omega,n) \int_{x',\theta'} \Psi(x,z;x',\theta') \delta[\Gamma_{\text{slit}}(z)] dx' d\theta' \\ &= d(\epsilon,\omega,n) \int_{\Gamma_{\text{slit}}{}^{(0)}} \Psi(x,z;x',\theta'(x')) dx'. \end{aligned} \tag{2.32}$$

One can definitely follow the same approach as in [21, 20] by first obtaining all necessary components on the computational mesh and then interpolating the solutions at the some sampling locations on the zero level set, as shown in figure 2. To initialize these functions in the original Eulerian framework, we have mentioned in the previous subsection that one has to somehow extend the initial conditions from one particular level set to the entire phase space. It is not trivial if the initial curve is an open segment as in the current case. One simple fix is to first extend the set Γ_{slit} to Γ and then initialize these components accordingly. For instance, one can extend A to the whole phase space by defining $A = 0$ for $x \notin \Omega_{\text{slit}}$. The description in the previous subsection can then be extended naturally. We can solve the same Liouville systems for the level set functions ϕ (2.24-1) and ψ (2.24-2), the traveltime function T (2.24-3), the amplitude function A (2.25-1) and also the Hessian M (2.25-2).

The main concern in applying this approach is the accuracy in solving the Liouville equation for the amplitude function. It is numerically challenging to maintain an accurate solution for $z > 0$. For example, if one is solving (2.25) using WENO-TVDRK methods as in typical level set methods, it could be difficult to maintain the shape discontinuity of A along the level set Γ. If one is solving $A(x,z)$ for $z > 0$ using the semi-Lagrangian method as in [22, 21, 20] to trace back along the characteristics, it could be tricky to accurately interpolate A on the initial mesh.

Moreover, in modeling propagation from only a small slit, this approach is not computationally efficient since the useful level set Γ_{slit} consists of only one or several small segment(s) in the whole phase space. It is therefore more desirable to apply a numerical scheme which can naturally and directly model the motion of open segment(s).

2.4.2 Initial Wavefield Decomposition

In this section, we will discuss the accuracy in recovering the incident wavefield at the slit using the Gaussian beam decomposition we described in the previous section. Without loss of generality, we consider a single slit centered at $x=0$ with width b and the domain is $x\in[-x_{\max},x_{\max}]$ with $x_{\max}>b/2$. With the formulation we described above, we decompose the initial wavefield into the sum of gaussian profiles

$$\begin{aligned} U(x,0) &= \chi_{\Omega_{\text{slit}}} \\ &\simeq \left(\frac{\epsilon\omega}{2\pi}\right)^{1/2}\int_{\Omega_{\text{slit}}}\exp\left[-\frac{\epsilon\omega}{2}(x-y)^2\right]dy \qquad (2.33)\\ &\simeq \left(\frac{\epsilon\omega}{2\pi}\right)^{1/2}\Delta x\sum_{i=-M}^{M}\exp\left[-\frac{\epsilon\omega}{2}(x-x_i)^2\right] \qquad (2.34)\end{aligned}$$

where $\epsilon=1/\omega\Delta x^2$, $\chi_{\Omega_{\text{slit}}}$ is the characteristic function which equals 1 if $x\in\Omega_{\text{slit}}=[-b/2,b/2]$ and 0 otherwise, x_i for $i=-M,\cdots,M$ is a uniform discretization of the interval Ω_{slit} and $\Delta x=b/2M$.

This discretized decomposition (2.34) is slightly different from the decomposition in the radial basis function approximation [5], in which one computes the projection of the initial function into the space spanned by some radial basis functions. For instance, one determines the coordinates/weights λ_i for $i=-N,\cdots,N$ by minimizing

$$\min_{\lambda_i}\left|\chi_{\Omega_{\text{slit}}}-\sum_{i=-N}^{N}\lambda_i\exp\left[-\frac{\epsilon\omega}{2}(x-x_i)^2\right]\right|^2 \qquad (2.35)$$

with $x_{\pm N}=\pm x_{\max}$. For this discontinuous initial profile, the interpolant

$$\sum_{i=-N}^{N}\lambda_i\exp\left[-\frac{\epsilon\omega}{2}(x-x_i)^2\right] \qquad (2.36)$$

unfortunately shows undesired oscillations near the discontinuity which does not decay to zero as $N\to\infty$. This Gibbs phenomenon has recently been carefully studies [12].

On the other hand, our approximation uses only $(2M+1)$ beams centered at $x_{-M}=-b/2,\cdots,x_M=b/2$, rather than $(2N+1)$ basis as in the radial basis function interpolation. Since the weight for each of these gaussian profiles is positive, the resulting approximation (2.34) does not show spurious oscillations nears the boundaries $x=\pm x_{\max}$ as in the Gibbs phenomenon.

Indeed, the approximation (2.34) will *always* generate non-zero incident wavefield for $|x|>b/2$. However, since each beams decays to almost zero when x is 3σ away from the center with $\sigma=1/\epsilon\omega=\Delta x$ is the standard deviation of the gaussian, the recovered wavefield (2.34) is well-approximated by zero for $||x|-b/2|>3\sigma$. In this sense, the support of the recovered incident field converges to the exact initial wavefield in the order of $O(\Delta x)$.

For other choice of ϵ, the parameter $(\epsilon\omega)$ places a very important role in the error from the initial condition decomposition. Using the terminology in the radial basis function interpolation, this parameter is also called the *shape parameter* which also controls how well-condition is the projection we discussed above. In the continuum limit (2.33), we have

$$\left(\frac{\epsilon\omega}{2\pi}\right)^{1/2}\int_{-b/2}^{b/2}\exp\left[-\frac{\epsilon\omega}{2}(x-y)^2\right]dy=\frac{1}{2}\left\{\mathrm{Erf}\left[\frac{1}{\sqrt{2}\sigma}\left(x+\frac{b}{2}\right)\right]-\mathrm{Erf}\left[\frac{1}{\sqrt{2}\sigma}\left(x-\frac{b}{2}\right)\right]\right\} \tag{2.37}$$

where $\mathrm{Erf}(x)$ is the (Gauss) error function given by

$$\mathrm{Erf}(x)=\frac{2}{\pi}\int_0^x\exp(-t^2)dt. \tag{2.38}$$

This decomposition also converges to $\chi_{\Omega_{\text{slit}}}$ as $\sigma\to 0$.

2.4.3 Numerical Approaches

Even though it is more computationally efficient to model the incident wavefield using an open curve in the phase space, it is numerically more challenging to compute its evolution in the Eulerian framework.

One simple method is to directly apply the level set method, [2] in the content of image analysis implicitly represented the open curves using the *centerline* of a level set function, i.e. the curve of interest is the zero level set. Numerically this is challenging since the level set function gives almost no zero value. To overcome this issue of numerical difficulties, the authors considered the μ-level set instead. But then the curve can never be recovered and there is always an $O(\mu)$ smoothed zone near the interface.

A second approach was the work of [35] for modeling spiral crystal growth. The idea was based on the level set method [28] where the author used the intersection of two level set functions to represent the codimension-two boundary of the open curve/surface. The curve/surface of interest was implicitly defined as the zero level set of one signed distance function at which the other one was positive, i.e. $S=\{x:\phi(x)=0 \text{ and } \psi(x)>0\}$. However, one had to define velocities for not only the level set function ϕ which represented the curve/surface of interest, but also the level set functions ψ which was used solely to define the codimension-two boundary. Moreover, the method proposed in [35] worked only for fixed-end curve and it is not clear how to define the velocity for ψ so that the evolution of the boundary satisfied certain given motion law. A generalization to this approach was proposed in [36] for constructing open surfaces from point cloud data. The method incorporated the method proposed in [6, 8] to allow motion of the boundary. Computationally, all these methods were not efficient since one has to solve not only one to get the implicit representation of the open curve/surface, but the number of PDEs, i.e. the number of the level set functions, equaled to the the codimension of the object.

Another approach was the vector distance function method [14] which extended the signed distance function of the level set method. The vector distance function was de-

fined as $\phi(\mathbf{x}) = \mathbf{x} - \mathbf{y}$ with $\mathbf{y}$ the closest point from the grid point $\mathbf{x}$ to the interface. Therefore, this vector valued function embedded not only the distance and the inside/outside information, but also the normal vector. Unfortunately, this representation required solving the same number of PDE's to the dimension of the space where the object is living, independent of the codimension of the object. In particular, the method required solving two PDEs for modeling open/closed curves/surfaces in $\mathbb{R}^2$.

Based on the grid based particle method we have introduced in [24], we have introduced a new numerical technique in [23] which can naturally model various motions of an open curve or an open surface in two dimensions and three dimensions. We will summarize the method in the next section.

3 The Grid-Based Particle Method (GBPM)

In this section, we introduce a newly developed numerical method which can naturally model evolution of open curves and can also solve these Liouville equations along with the motion. We will first summarize the method in Section 3.1 and then we will explain how the open curves motion can be taken care of in Section 3.2 and how this method can naturally solve the Liouville equation in Section 3.3.

3.1 The Method

In this section, we give a general recipe of the grid based particle method. For a complete description of the algorithm, we refer the readers to [24].

In [24] and also in this paper, we represent the interface by meshless particles which are associated to an underlying Eulerian mesh. In our current algorithm, each sampling particle on the interface is chosen to be the closest point from each underlying grid point in a small neighborhood of the interface. This one to one correspondence gives each particle an Eulerian reference during the evolution. The closest point to a grid point, $\mathbf{x}$, and the corresponding shortest distance can be found in different ways depending on the form in which the interface is given.

At the first step, we define an initial computational tube for active grid points and use their corresponding closest points as the sampling particles for the interface. A grid point $\mathbf{p}$ is called **active** if its distance to the interface is smaller than a given **tube radius**, ϵ, and we label the set containing all active grids Y. To each of these active grid points, we associate the corresponding closest point on the interface, and denote this point by $\mathbf{y}$. This particle is called the **foot-point** associated to this active grid point. This link between the active grid points and its foot-points is kept during the evolution. Furthermore, we can also compute and store certain Lagrangian information of the interface at the foot-points, including normal, curvature and parametrization, which will be useful in various applications.

As a result of the interface sampling, the density of particles on the interface will be roughly inversely proportional to the local grid size. This relation provides an easy

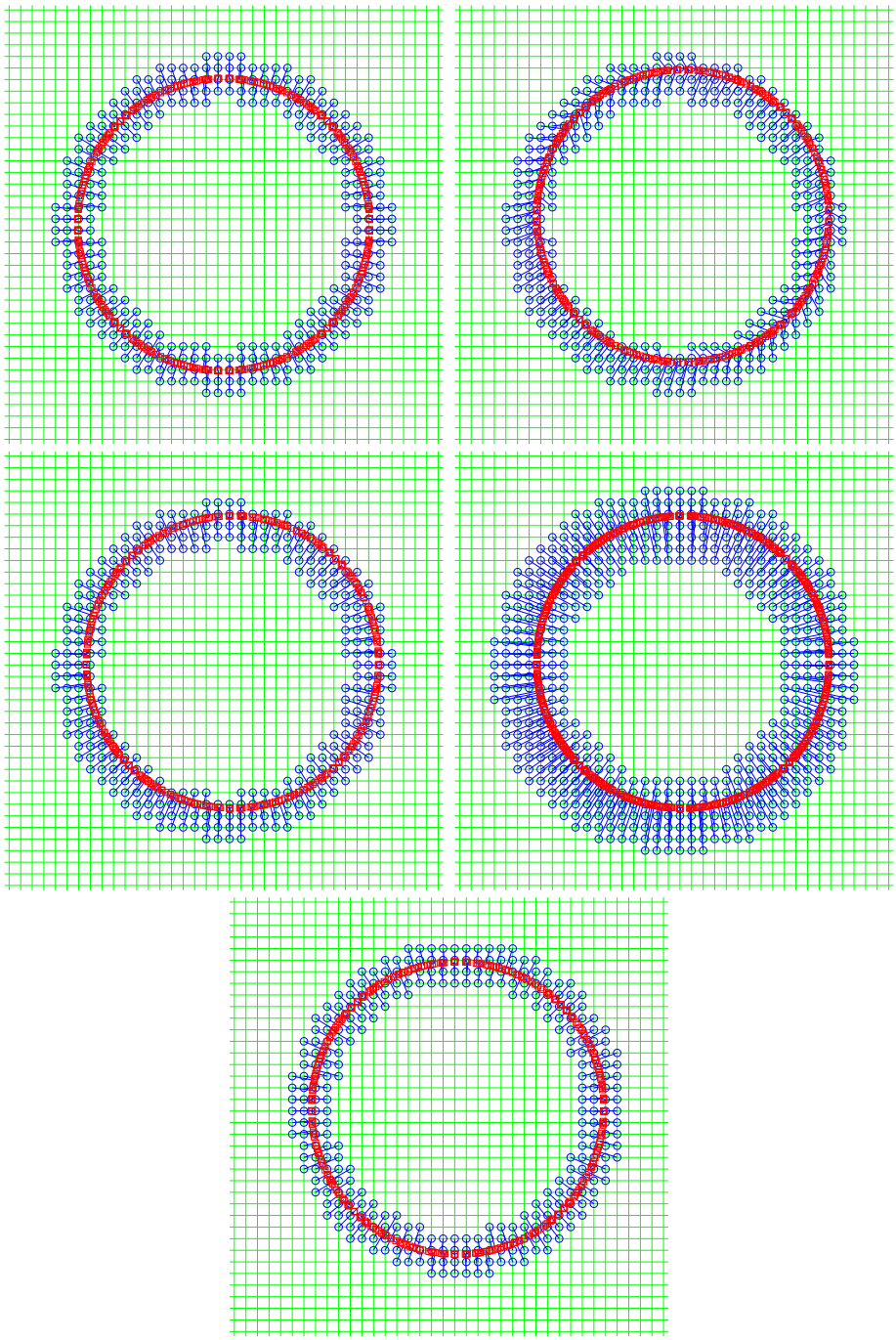

Figure 3: Grid Based Particle Method. From left to right: (a) Initialization, (b) after motion, (c) after re-sampling, (d) after activating new grid points with their foot-points, (e) after inactivating grid points with their foot points.

adaptive approach in the current grid based particle method. In some regions where one wants to resolve the interface better by putting more marker particles, one might simply locally refine the underlying Eulerian grid and add the new foot-points accordingly.

This initial set-up is illustrated in figure 3 (a). We plot the underlying mesh in solid line, all active grids using small circles and their associated foot-points using squares. On the left most sub-figure, we show the initial set-up after the initialization. To each grid point near the interface (blue circles), we associate a foot-point on the interface (red squares). The relationship of each of these pairs is shown by a solid line link. In practice, we do not necessary use such a thick computational tube. Since the thicker the tube, the more over-sampling of the interface. Usually, we use $\epsilon = 1.1h$ which already gives a relatively good sampling.

To track the motion of the interface, we move all the sampling particles according to a given motion law. This motion law can be very general, but in this paper, we will only concentrate on the motion under an external velocity field given by $\mathbf{u} = \mathbf{u}(\mathbf{y})$. Since we have a collection of particles on the interface, we simply move these points just like all other particle-based methods, which is simple and computationally efficient. We can simply solve a set of ordinary differential equations using high order scheme which gives very accurate location of the interface.

It should be noted that a foot-point $\mathbf{y}$ after motion may not be the closest point on the interface to its associated active grid point $\mathbf{p}$ anymore. For example, figure 3 (b) shows the location of all particles on the interface after the constant motion $\mathbf{u} = (1,1)^T$ with a small time step. As we can see, these particles on the interface are not the closest point from these active grid points to the interface anymore. More importantly, the motion may cause those original foot-points to become unevenly distributed along the interface. This may introduce both stiffness, when particles are getting together, and large error, when particles are getting apart. To maintain a quasi-uniform distribution of particles, we need to resample the interface by recomputing the foot-points and updating the set of active grid points (Y) during the evolution. During this resampling process, we locally reconstruct the interface, which involves communications among different particles on the interface. This local reconstruction also provides geometric and Lagrangian information at the recomputed foot-points on the interface.

The key step in the method is a least square approximation of the interface using polynomials at each particle in a local coordinate system, $\{(\mathbf{n}')^{\perp}, \mathbf{n}'\}$, with $\mathbf{y}$ as the origin, figure 4 (a). Using this local reconstruction, we find the closest point from this active grid point to the local approximation of the interface, figure 4 (b). This gives the new foot-point location. Further, we also compute and update any necessary geometric and Lagrangian information, such as normal, curvature, and also possibly an updated parametrization of the interface at this new foot-point. For a detail description, we refer interested readers to [24].

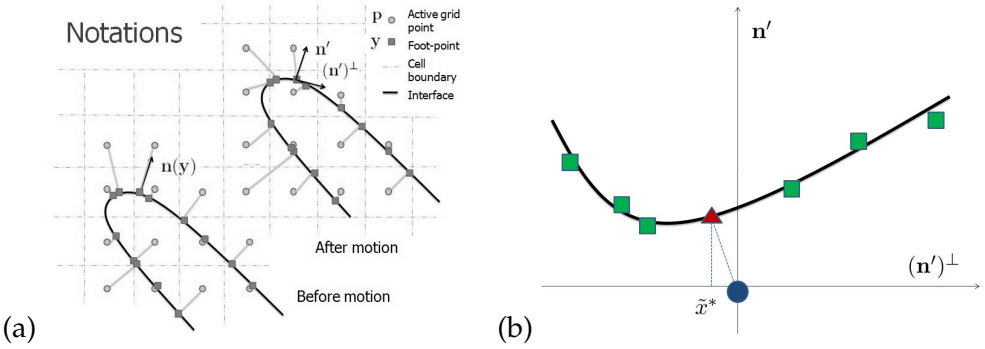

Figure 4: (a) Definition of a local coordinates. (b) Local reconstruction of the interface using the foot-points (green squares). The new foot-point (red triangle) associated to the active grid point (blue circle) is obtained by least square fitting a polynomial.

3.2 The GBPM for Open Curves Evolutions

In this section, we will briefly summarized [24] and discuss how our algorithm can model the motion of an open curve (in 2 dimensions). The main idea is to explicitly keep track of the motion of the end-points of the open curve, and then to enforce this condition on the boundary locations in the local reconstruction step of the grid-based particle method we described in the previous subsection.

3.2.1 Representation

As defined before, any grid point which is in a ϵ-neighborhood of the interface is called active grid point. In figure 5, we demonstrate a typical scenario near an end-point of an open curve. Given an open curve, we first collect active grid points which are within the ϵ-neighborhood. Then, for each of these active grid points we find the corresponding closest points on the open curve.

Away from the boundary point (green sun-symbol), the set-up is exactly the same as before. If an active grid point has a distance greater than ϵ away from the boundary (green sun-symbol), we simply project the grid point (red square) onto the surface locally reconstructed by the least square fitting. This gives the associated foot-point (red circle) on the surface.

For a grid point within the ϵ-neighborhood of the boundary, we assign it with **two** foot-points. One is the closest point from the grid point to the open surface, while the second one is the closest point from the active grid point to the *closed boundary* and we will call this second foot-point the boundary-point. In two dimensions, the second foot-point is just the end-point itself, as shown in figure 5.

Note that these two foot-points could be the same or could be different. In figure 5, we plot these special grid points using blue triangles or green squares. Consider the blue triangles, one of their associated foot-points is still obtained by local least square

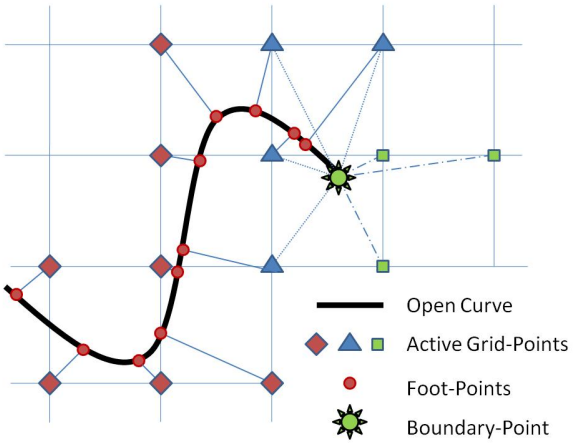

Figure 5: Representation of the open surface and the boundary in the Grid-Based Particle Method. Away from the boundary-point (the green sun-symbol), the representation is the same as in [24]. Each active grid point (red diamonds) is associated to its closest point on the interface (red circles). Near the boundary-point, each active grid point (blue triangles and green squares) is associated to its closest point (red circles or green sun-symbol) and also the closest boundary point (green sun-symbol).

approximation of the interface, which is plotted using red circles. Since these blue triangle active grid points are within ϵ from the end point (green sun-symbol), their second foot-points are also activated which are the closest boundary points (the connectivity is plotted using a dotted line). In figure 5, we plot this type of active grid points using green squares and the connectivity between the active grid points and their foot-points using a dashed-dotted line.

3.2.2 Motion and Resampling

Now we discuss how our algorithm incorporates this boundary information in the evolution step and the resampling step. As before, the motion phase of the algorithm is relatively straight-forward. We simply move all sampling points (including both the closest points and the boundary-points) as in the usual Lagrangian type methods. The motion law of the closest-points can be very general. We can naturally deal with the motion by an external velocity field or geometrical motions such as motion by the mean or the Gaussian curvature. The motion law imposed on boundary-points can be explicitly given or can be determined by local geometry of the *boundary* such as the curvature or the torsion, which can be easily computed from local reconstruction of the boundary as described in the previous section.

For two dimensional cases, there is no need to resample end-points of the open curve since they are just explicitly tracked points. The resampling of the open surface near the boundary requires more care. Away from the boundary, the resembling step follows the procedures in standard grid based particle method. However, near the boundary, we

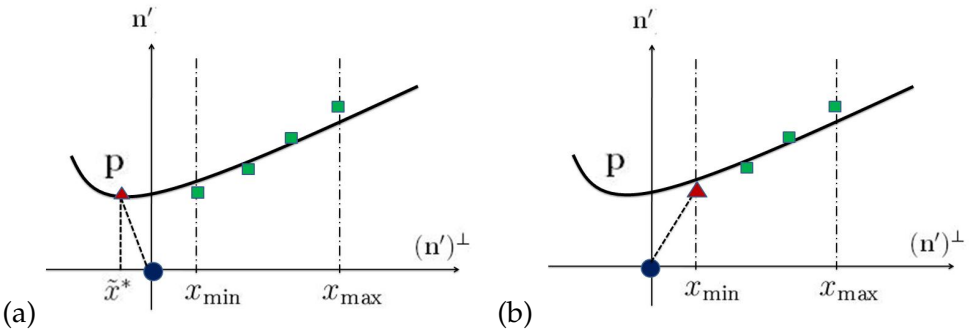

Figure 6: (a) In the original algorithm [24], any potential new foot-point (red triangle) will be rejected if $x^* \notin [x_{\min}, x_{\max}] = [\min(x_j), \max(x_j)]$. (b) In the new algorithm, we associate the new closest point to the closest boundary-point if the corresponding active grid point is close to the boundary. In this plot, we associate the active grid point (blue circle) to the particle corresponding to $x_{\min}$ (red triangle) assuming it is a boundary-point.

need to take into account the boundary of the open surface.

The local reconstruction phase of the algorithm is similar as before. For each of the active grid point **p**, we consider its neighboring active grids and collect a set of their corresponding closest points and, if any, also a separate set of their corresponding boundary-points. If **p** is close to the boundary of the open surface, its neighboring active grid point might be assigned **two** foot-points which might or might not be the same (the blue triangles and the green squares in figure 5, respectively). We will distinguish these two types of foot-points in this local reconstruction step.

If the set of boundary-points is empty, we will simply use the set of closest points for local reconstruction, as in the original algorithm in [24]. Otherwise, we will form a set of sampling points for local reconstruction using both the set of closest points and also the set of boundary-points. These sampling points have to satisfy the following two conditions. The first criteria is the same as what we have proposed in [24] that any two sampling points should be at least of $O(h)$ away, where h is the local mesh size. This removes any redundant information in the sampling points. The second constraint is that boundary-points in the sampling set should define at least parts of the boundary of $\tilde{\Omega}$, where $\tilde{\Omega}$ is the convex hull formed by the projection of the sampling points on the tangent plane. This is the first place where we incorporate the boundary information in the local reconstruction.

In two dimensions, here is the way to construct this sampling set from both the closest points and the boundary-points. The set of the sampling point starts with the set of the closest points, for which by default any two of these particles are of at least $O(h)$ away from each other. Then for each boundary-point, we check if it is $O(h)$ away from all of the sampling points or not. If not, then we will reject that particular boundary-point and then repeat the procedure with the next boundary-point. Otherwise, in the local

coordinates system $\{(\mathbf{n}')^{\perp},\mathbf{n}'\}$ where we denote the boundary-point by $(\hat{x},\hat{y})$ and the set of the accepted sampling points by (x_j,y_j), we check if $\hat{x}\in[\min(x_j),\max(x_j)]$. If not, then we will add this boundary-point to the list of the sampling point. Otherwise, we will use this boundary-point to replace the sampling point corresponding to either $\min(x_j)$ or $\max(x_j)$, whichever closer to $\hat{x}$.

Now, with these sampling points, we construct a local least square fitting and we denote it by $y=f(x)$. To determine the new closest point, we minimize the distance from the grid point $\mathbf{p}$ to the function $y=f(x)$. If the minimum is attained at $x^*\in[\min(x_i),\max(x_i)]$, we follow the same procedure as in [24] and determine the new closest point $(x^*,f(x^*))$, accordingly. In the previous algorithm, we deactivated any grid point if this new foot-point leads to an extrapolation, i.e. if $x^*\notin[\min(x_i),\max(x_i)]$, figure 6 (a). For active points near the boundary, we again enforce the boundary information at this step of the algorithm. We now go back and check if the set of boundary-points is non-empty, i.e. if any of the active grid points in the neighborhood is of the blue triangle or the green square type as in figure 5. If so, we will assign x^* to this boundary-point, for example $x^*=x_{\min}$ as shown in figure 6 (b). If none of the neighboring active grid points is associated to a boundary-point, we will simply deactivate this active grid point as in [24].

All other steps in our algorithm will be the same as described in [24]. We approximate any Lagrangian information associated to this particle using the local reconstruction of the surface. For example, the normal vector at this new foot-point is approximated by the normal vector of the local reconstruction at $\mathbf{x}^*$. The curvature and the global parametrization can also be updated accordingly.

3.3 The GBPM for Solving Liouville Equations

In this section, we consider $f:\Sigma(t)\to\mathbb{R}$ defined on the surface $\Sigma(t)$ represented by our quasi-uniformly distributed but unorganized particles. Considering the following Liouville equation, we have the following ODE defined along each characteristic

$$\frac{Df(\mathbf{y}(t))}{Dt}=g(t,\mathbf{y}(t),f(\mathbf{y}(t))), \tag{3.1}$$

where $D/Dt=\partial/\partial t+\mathbf{u}\cdot\nabla$ is the material derivative along any trajectory of a particle $\mathbf{y}(t)$ on the interface, and g is the source term defined only on the surface. For instance, if f is one of the level set functions ϕ or ψ, then the source term g is simply zero and this implies that the quantity f in this case should be preserved along any particle trajectory. If f is one of T, $\mathcal{A}$ and $\mathcal{M}$, the source term g will be modified according to (2.24) and (2.25).

There are two main steps in using the GBPM for solving the advection-reaction equation. We first solve the advection-reaction equation along with the particle trajectory in the motion phase. Then for each sampling particle in the resampling step, we use again least square fitting polynomials to approximate f at new foot-point locations. In the remaining subsections, we will discuss these two main steps in details.

3.3.1 Motion Phase

Solving this Liouville equation is relatively straight-forward in the motion phase of our formulation. Since we are representing the interface $\Sigma(t)$ using Lagrangian particles, we can simply solve a system of ODE's to update the function value f carried by each particle. Denoting $\mathbf{y}_i(t^n)$ the location of the foot-point associated to an active grid point $\mathbf{x}_i$ at the time $t=t^n$. According to the motion $\mathbf{u}=\mathbf{u}(\mathbf{y}_i)$, we solve the following system of ODE

$$\begin{aligned} \frac{d\mathbf{y}(t)}{dt} &= \mathbf{u}(\mathbf{y}(t)) \\ \frac{Df(\mathbf{y}(t))}{Dt} &= g(t,\mathbf{y}(t),f(\mathbf{y}(t))). \end{aligned} \tag{3.2}$$

for one timestep from t^n to t^{n+1} with the initial conditions $\mathbf{y}(t^n)=\mathbf{y}_i(t^n)$ and $f(\mathbf{y}(t^n))=f(\mathbf{y}_i(t^n))$. This system can be solved easily using any ODE integrator such as the TVD-RK method [34]. To improve the stability, we can also apply any implicit schemes in a straight-forward way if the source term does not depend on the local geometry of the surface. We will study and develop implicit schemes for solving geometry-depending PDE on an evolving surface in a later paper.

These new particle locations indeed sample the surface $\Sigma(t^{n+1})$ at t^{n+1}. Note however that since these particles are in general not the closest points from their associated active grid points, we denote these solutions at t^{n+1} by $\mathbf{y}_i^*(t^{n+1})$ and $f(\mathbf{y}_i^*(t^{n+1}))$, rather than $\mathbf{y}_i(t^{n+1})$ and $f(\mathbf{y}_i(t^{n+1}))$.

3.3.2 Resampling Phase

The next step in the algorithm is to resample the surface by recomputing the closest point from an active grid point to the interface by locally reconstructing the surface using least square fitting. For solving the Liouville equation, we have to update the function value at the new foot-point location $\mathbf{y}_i(t^{n+1})$ using the function values at $\mathbf{y}_j^*(t^{n+1})$. This is essentially an approximation problem. Given $f(\mathbf{y}_j^*(t^{n+1}))$ for $j=1,\cdots,m$, we need to approximate $f(\mathbf{y}_i(t^{n+1}))$. In this paper, we consider the local coordinates at $\mathbf{y}_i^*(t^{n+1})$ and approximate the function value on the tangent plane. As an example, we here discuss in details the two dimensional formulation. Higher dimensions extension is relatively simple. In the local coordinate $\{(\mathbf{n}')^\perp,\mathbf{n}'\}$ with $\mathbf{n}'$ the normal vector associated to the foot-point $\mathbf{y}_i(t^n)$, we express the function f in terms of this local coordinates $(\tilde{x},\tilde{y})$. This gives

$$f(x,y)=f(\tilde{x},\tilde{y}(\tilde{x}))=f(\tilde{x}) \tag{3.3}$$

where $\tilde{y}(\tilde{x})$ is the least square polynomial we used to locally approximate the interface. Let $\tilde{x}^*$ be the minimizer which leads to the location for the new foot-point, figure 7 (a), we have the following approximation problem. Given m data points $(\tilde{x}_j,f(\tilde{x}_j))$ for $j=1,\cdots,m$, we want to approximate $f(\tilde{x}^*)$. Various interpolation or approximation methods could be used. In the current formulation, we again use the least square technique and determine

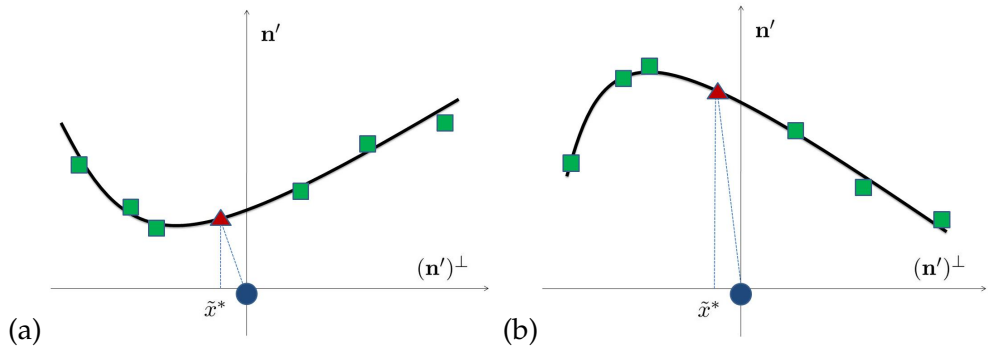

Figure 7: (a) Local reconstruction of the interface using the foot-points (green squares). The new foot-point (red triangle) associated to the active grid point (blue circle) is obtained by least square fitting a polynomial. (b) Approximating $\tilde{f}(\tilde{x}^*)$ (red triangle) by least square fitting a polynomial using $f(\tilde{x}_j)$ (green squares).

a polynomial approximation $\tilde{f}$ to the function f according to the data points. Then the function value at the new foot-point is given by $\tilde{f}(\tilde{x}^*)$ as shown in figure 7(b), i.e.

$$f(\mathbf{y}_i(t^{n+1})) = \tilde{f}(\tilde{x}^*). \tag{3.4}$$

3.4 Gaussian Beam Summation

Once we have obtained all necessary components at the foot-points, we can construct the resulting wavefield generated by these sampling beams.

On the right subplot in figure 8, we have demonstrated a typical sampling scenario obtained by the grid based particle method. In figure 2, the sampling particles are obtained by finding the zero's of the level set function at each x_i using linear interpolations. In the grid base particle method, these sampling particles are closest points from the underlying uniform mesh. There is a fundamental difference between these two solutions. Using the pure Eulerian formulation as in figure 2, we immediately obtain for any grid point x_i all arrival-angle(s) $\theta(x_i)$, and also the corresponding arrival-time(s) and other necessary components for constructing the induced wavefield. In the grid based particle method, on the other hand, the sampling is only quasi-uniform. The sampling locations depend on not only the underlying mesh size Δx, but also the geometry of the curve. To compute all arrival-angles and their corresponding arrival-times at a particular receiver location x_i, we need to further interpolate all sampling foot-points. However, we will not further study the implication of this difference in the sampling since we can still eventually obtain the overall wavefield on a **uniform** mesh in the real space.

For each of the foot-points (x_i,θ_i) on the open curve at a given z, we first compute the wavefield Ψ induced by this particular arrival beam using (2.20). One could definitely speed up the computations by looking at only a small neighborhood of the central beam

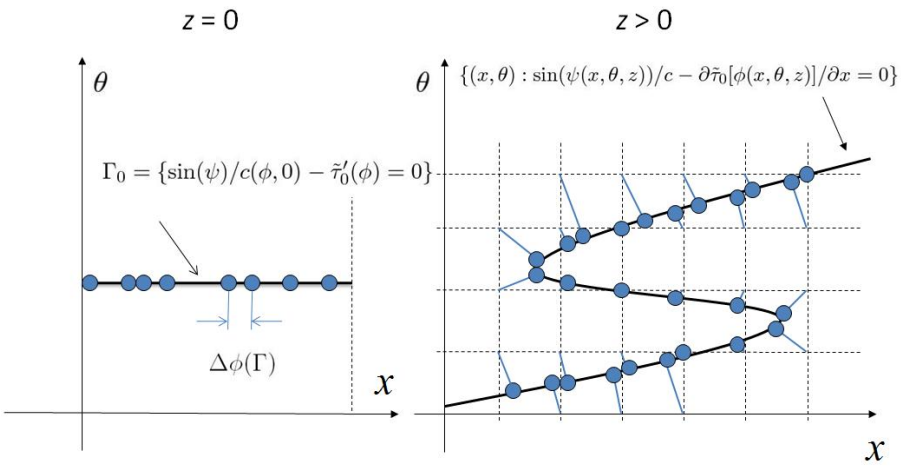

Figure 8: The sampling particles (blue dots) of the level set in the grid based particle method. Note the difference on the sampling from figure 2.

since the magnitude of the wavefield decays exponentially away from each of these beam anyway [39]. But in this current implementation, we do not study the relationship of applying such a mask function with the accuracy of the final solution, and we simply determine the induced wavefield everywhere in the computational domain.

The next step is to sum up all these contributions according to the initial parametrization of all arrival beams, i.e. summing up these beams according to (2.32). Associated to all foot-points, we have the level set function ϕ which acts as a natural parameterization in the case since the incident rays can be parametrized by their incident location x' as in (2.32). As shown in the left subplot in figure 8, the function value of ϕ essentially provides the takeoff location of the arrival beam.

Approximating the integral (2.32), we need to determine the weight for the wavefield induced by each arrival beam. We first sort these ϕ_i at these foot-points (x_i,θ_i) for $i=1,\cdots,I$. It is possible that several foot-points might have the same ϕ_i. For example, considering the initial setup where we consider a horizontal curve. Active grid points from above and below the interested segment will coincide to the same points, giving the same ϕ_i for multiple foot-points. In this case, we first eliminate the redundant foot-points in this summation process and average all carrying function values among these redundant particles. Then, the weight for each of these distinct arrival beams will be computed by the average of the distances between the two neighboring ϕ_i's. Mathematically, assuming ϕ_i is sorted, we have $w_j = \Delta\phi_j = |\phi_{j+1} - \phi_{j-1}|/2$.

3.5 Algorithm

To end this section, we first summarize the whole algorithm in obtaining diffraction patterns using Eulerian Gaussian beams and the grid based particle method. Then we will

discuss the computational complexity of the proposed algorithm and will compare it with different approaches.

Algorithm (diffraction pattern using EGB and GBPM):

1. Initialization. Collect all grid points in a small neighborhood of the open curve. From each of these grid points, compute the closest point on the interface. Initialize ϕ, ψ, $\mathcal{A}$, $\mathcal{M}$ and T according to (2.18) and (2.24).
2. Motion. Move all foot-points according to a given motion law given by (2.6).
3. Updating necessary components. Update ϕ, ψ, $\mathcal{A}$, $\mathcal{M}$ and T according to (2.24) and (2.25) along the motion trajectories as described in Section 3.3.1.
4. Re-Sampling. For each active grid point, re-compute the closest point to the interface reconstructed locally by those particles after the motion in step 2. Approximate ϕ, ψ, $\mathcal{A}$, $\mathcal{M}$ and T at all new foot-points using least square fitting as described in Section 3.3.2.
5. Updating the computational tube.
6. Construct individual wavefields. For each foot-point, compute the induced wavefield using (2.20).
7. Construct overall wavefield. Determine the weight for each individual wavefield as described in Section 3.4.
8. Iteration. Repeat steps 2-7 until the final computational time.

Let N be the number of grid points in each direction in the phase space. The open curve in the GBPM can be represented by $O(N)$ points. This significantly drops the order from $O(N^2)$ comparing to the approach in [21, 20] as described near the end of Section 2.4.1. The motion step according to (2.6) and the evolution step according to (2.24) and (2.25) involves only ODE solvers. For $O(N)$ points in the phase space, the overall computational complexity is still $O(N)$ for these two phases for one Δz step. To compute these quantities up to a fixed final level z_f, the overall computational complexity is $O(N^2)$. To determine the overall wavefield for each given z, we first construct the individual wavefield according to (2.20) and then sum up all individual wavefield according to (2.32). The computational complexity is $O(N)$ for each beam and therefore $O(N \cdot N) = O(N^2)$ for all $O(N)$ beams. If the wavefield is necessary only on the final level z_f, one might skip steps 6 and 7 in the above algorithm for all intermediate steps and so the overall computational complexity is of only $O(N^2)$. If the wavefield is necessary for all z-level,

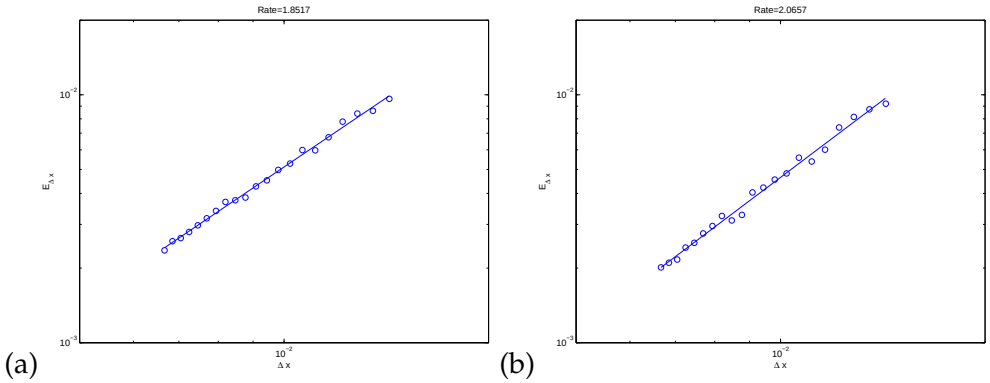

Figure 9: Convergence of solving a PDE on an evolving surface using (a) $E_{\Delta x,2}$ and (b) $E_{\Delta x,\infty}$.

the computational complexity is $O(N^3)$. Even with $\Delta x = O(\omega^{-1/2})$, the overall computational complexity is of only $O(\omega^{3/2})$, which is still significantly better than usual finite difference methods.

4 Examples

4.1 Accuracy in Solving PDE on an Evolving Surface

In this first example, we will study the accuracy and the convergence of solving an advection-reaction equation using the grid based particle method. We consider solving

$$\begin{aligned} \frac{Df}{Dt} &= [4\pi\cos(4\pi t)]f \\ f(0,\theta) &= \sin(2\theta) \\ \tan\theta &= \frac{y-0.25}{x-0.25} \end{aligned} \tag{4.1}$$

on an evolving circle under the velocity field $(u,v) = (1,1)$. The circle is initially centered at $(0.25,0.25)$ with radius 0.2. We compute the solution of f at $t = 0.5$ and compare it with the exact solution on the circle finally centered at $(0.75,0.75)$ with the same radius 0.2

$$\begin{aligned} f_{\text{exact}}(t,\theta) &= \sin(2\theta)\exp[\sin(4\pi t)] \\ \tan\theta &= \frac{y-0.25-t}{x-0.25-t}. \end{aligned} \tag{4.2}$$

All quadratures are done using the TVD-RK3 method.

In figure 9, we plot the errors in the solution using the following two- and infinity-

norms.

$$\begin{aligned} E_{\Delta x,2} &= \sqrt{\int_\theta |f(0.5,\theta)-f_{\text{exact}}(0.5,\theta)|^2 d\theta} \\ E_{\Delta x,\infty} &= \max_\theta |f(0.5,\theta)-f_{\text{exact}}(0.5,\theta)| \end{aligned} \tag{4.3}$$

for different Δx. For each active grid point, we first compute the exact value of f at the exact closest point from the grid location to the circle. We then compare it with the computed function value at the foot-point. To calculate the overall error, we sum these pointwise errors using the Trapezoidal integration.

The error consists of the following two parts. The first part is the error we made in calculating the foot-point location. Numerically, the foot-point only approximates the closest point locations since there is error we made in the local reconstruction. However, as studied in [24], such error is of $O(\Delta x^3)$ when using a local quadratic approximation. The second contribution is the error we made in solving the ODE and approximating the function on the interface in the resampling step. Since we are using the TVD-RK3 which is third order accurate for each time step, the overall accuracy at a fixed final time is therefore $O(\Delta x^3 \cdot \Delta t) = O(\Delta x^3 \cdot \Delta x^{-1}) = O(\Delta x^2)$. This explains the second order convergence (1.85, 2.06) in figure 9.

4.2 Single or Double Slit Diffraction in a Homogeneous Medium

In this example, we consider diffraction patterns in a homogeneous medium. These are relatively simple cases where good analytical explicit approximations are available. The first example is the single slit diffraction with the aperture centered at $x=0$ having size equals to $b=0.1$. We assume that the incident wave is a plane wave with the frequency $\omega=256\pi$. Since the Liouville equation has $u=v=0$ in the phase space, we concentrate our computations on the domain $x\in[-0.1,0.1]$ and $\theta\in[-1.5,1.5]$ using a uniform underlying mesh of 257 grids in each direction.

For these simple cases, the motion law (2.6) is reduced to $\dot{x}=\tan\theta$ and $\dot{\theta}=0$. For $\theta(z=0)=0$ (corresponding to the plane wave passing through the slit), we have $x(z)=x_0$ and $\theta(z)=0$. This means that an open segment stays the same open segment in the phase space. When projected onto the physical space, the open segment just translates in the z-direction without any stretching/folding in the x-direction.

In figure 10 (a), we show our computed intensity field defined as $I=|U|^2$ for z up to 3. We have compared our solution at $z=z_f=3$ with some well-known approximations to this single slit diffraction problem [13]. In figure 10 (b), we plot the intensity at $z=z_f$ together with the Fraunhofer diffraction formula given by

$$I(\theta) \simeq I(0)\left(\frac{\sin\beta}{\beta}\right)^2, \tag{4.4}$$

where $\tan\theta = x/z_f$, $\lambda = 2\pi/\omega$, and $\beta = \pi b \sin\theta/\lambda$. This approximation is obtained by considering the asymptotic solution to the Fresnel-Kirchhoff formula as $z_f \to \infty$ with the

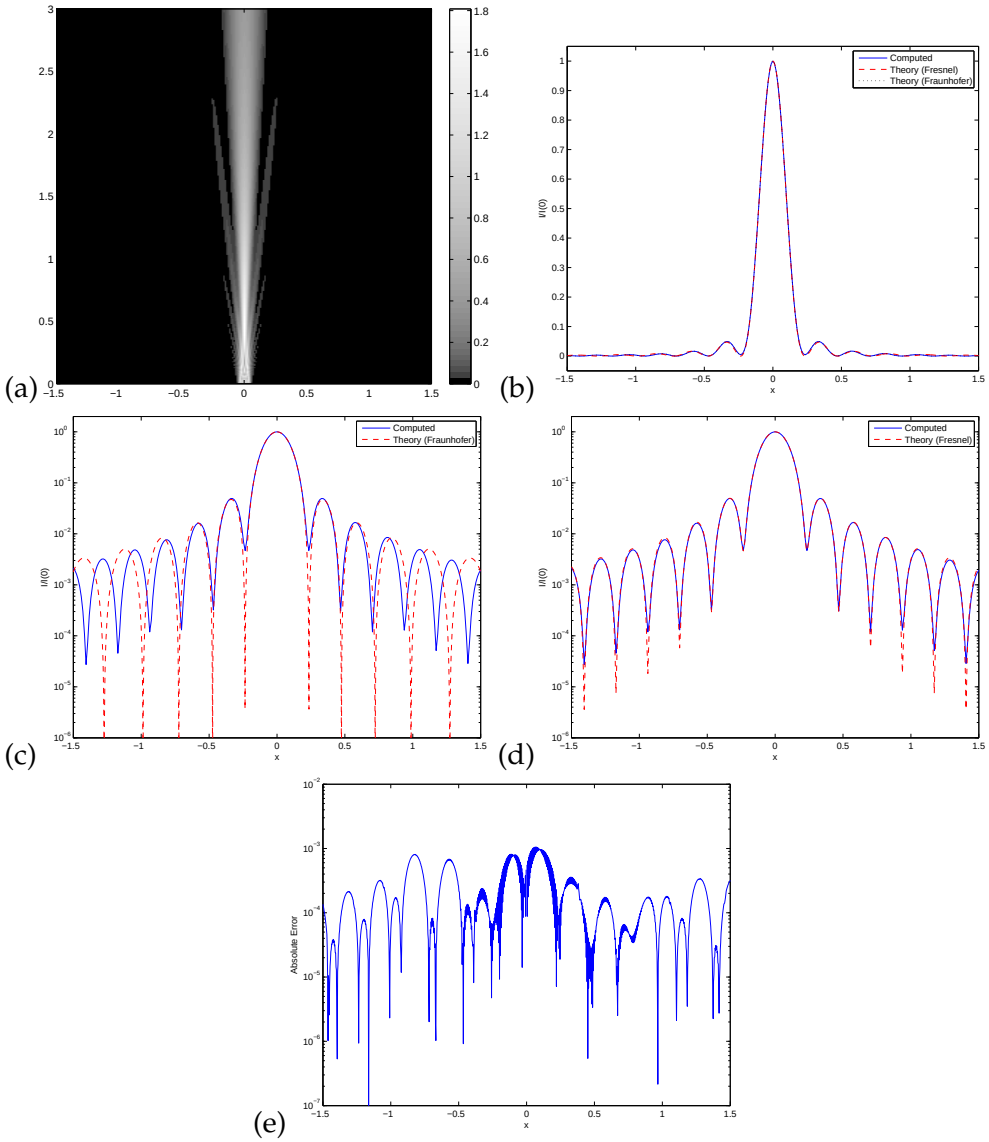

Figure 10: Single slit diffraction in homogeneous medium. The aperture is $b=0.1$ with an incident plane wave frequency $\omega=256\pi$. (a) The intensity field using Eulerian Gaussian beams summation. (b) The intensity at $z=z_f=3\gg b=0.1$. (c) Comparison with the Fraunhofer's solution (dashed line) in the log-scale. These two solutions acceptably match with each other for the middle region where $|x|$ is small. (d) Comparison with the Fresnel's solution (dashed line) in the log-scale. (e) The absolute difference between the computed intensity and that from the Fresnel approximation.

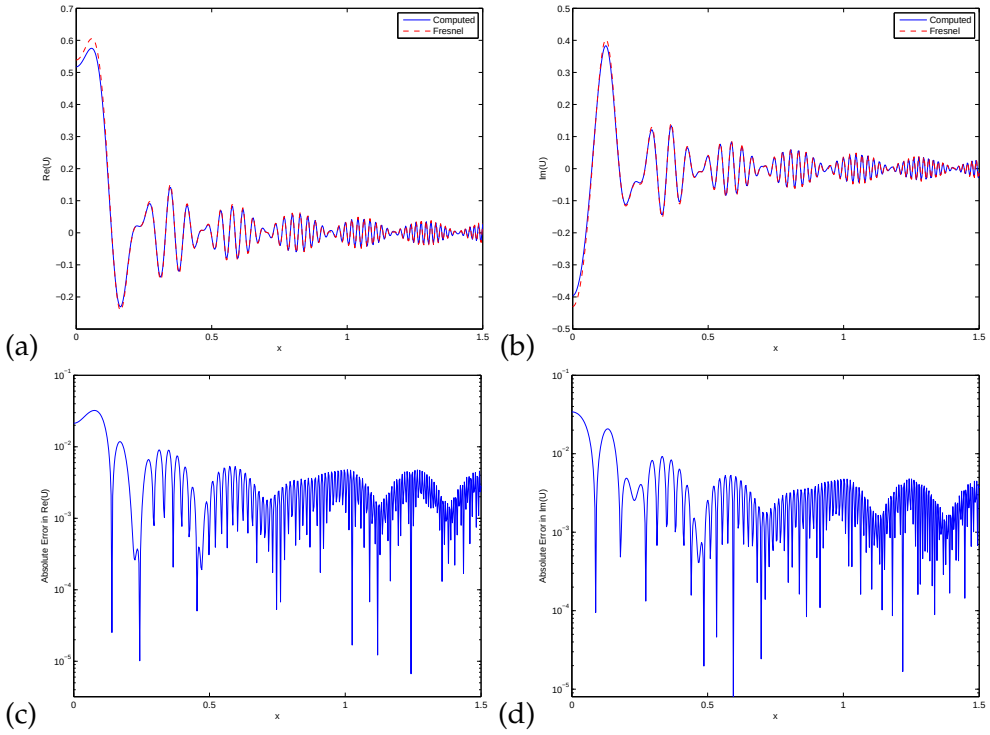

Figure 11: Single slit diffraction in homogeneous medium. The aperture is $b=0.1$ with an incident plane wave frequency $\omega=256\pi$. (a) The real part of the wavefield on $z=3$ and $0<x<1.5$. (b) The imaginary part of the wavefield on $z=3$ and $0<x<1.5$. (c) The absolute difference between the solution in (a) and that from the Fresnel approximation. (d) The absolute difference between the solution in (b) and that from the Fresnel approximation.

small $|x|$, approximation. To better compare the Eulerian Gaussian beams solution with the Fraunhofer solution, we have also plotted the intensity in the log-scale, figure 10 (c). Our computed solution matches well with this analytical intensity in the middle portion. For larger $|x|$, our computed solution starts to deviate from the approximation given in (4.4). The locations of the first few maxima and minima match very accurately. However, the corresponding intensity at these minima are quite different. Theoretically, the Fraunhofer diffraction gives zero intensity at these minima which is accurate only asymptotically as $z_f \to \infty$.

A better approximation is obtained by considering the Fresnel approximation which simplifies the Fresnel-Kirchhoff formula and gives

$$I(x) \simeq I(0)|C(x)+iS(x)|^2, \tag{4.5}$$

where $C(x)$ and $S(x)$ are the Fresnel integrals given by

$$\begin{aligned} C(x) &= \int_0^{v(x)} \cos\left(\frac{\pi w^2}{2}\right) dw \\ S(x) &= \int_0^{v(x)} \sin\left(\frac{\pi w^2}{2}\right) dw \\ v(x) &= \sqrt{\frac{2}{\lambda z_f}}\left(\frac{b}{2}-x\right). \end{aligned} \tag{4.6}$$

This solution more accurately approximates the Fresnel-Kirchhoff formula than the Fraunhofer's approximation for finite $z_f \ll \infty$. The Fraunhofer formula predicts that the solution has zero intensity at minima when $\beta = m\pi$ for $m = 0, \pm 1, \pm 2, \cdots$. For finite z_f, this observation is not true and has to be corrected using the Fresnel diffraction. As seen in 10 (d), our solution not only locates similar maxima/minima locations, but also gives similar nonzero intensity at these maxima/minima as obtained by the Fresnel solution (4.5), as shown in (e). In figure 11, we have directly compared the computed wavefield on $z=3$ to that from the Fresnel approximation given by

$$U(x,y) = -\frac{3i}{4}\exp\left(\frac{i\pi}{4}+\frac{2\pi i z_f}{\lambda}\right)[C(x)+iS(x)]. \tag{4.7}$$

These two solutions match very well.

A slight more complicated situation is the double slit diffraction. In this example, we have used $a=0.1$ and $b=0.05$. To resolve the incident wave from each slit using the same number of Gaussian beams, we have doubled the number of grid to 513 in each direction of the phase space. We use the same frequency $\omega = 256\pi$ and compute the solution at the same $z_f = 3$.

Figure 12 shows our computed solution together with the Fraunhofer diffraction formula and the Fresnel approximation. Similar to the single slit diffraction, our solution matches well with the Fraunhofer approximation for small $|x|$ and matches extremely

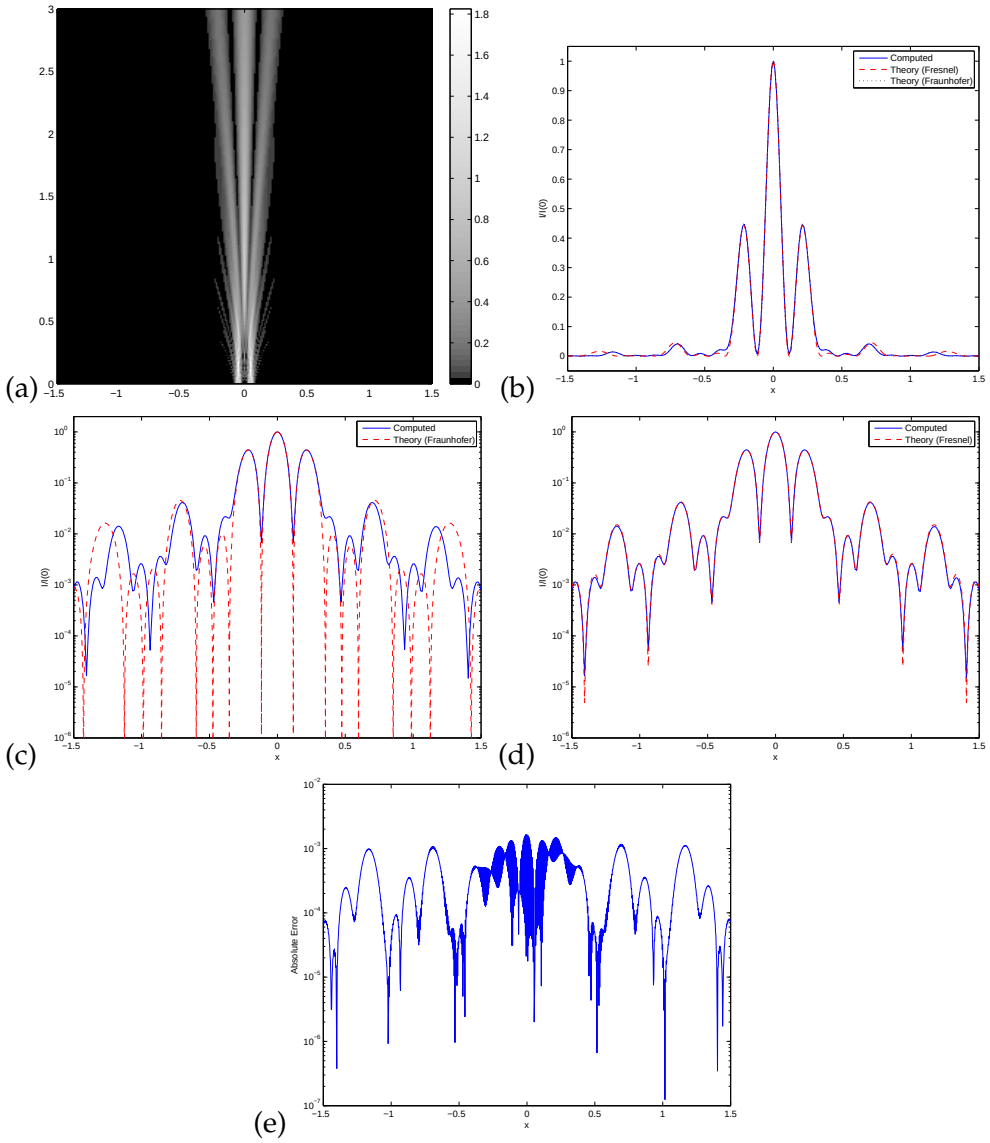

Figure 12: Double slit diffraction in homogeneous medium. The distance between two slits is $a = 0.1$ and the aperture of each slit is $b = 0.05$ with an incident plane wave frequency $\omega = 256\pi$. (a) The intensity field using Eulerian Gaussian beams summation. (b) The intensity at $z = z_f = 3$. (c) Comparison with the Fraunhofer's solution (dashed line) in the log-scale. These two solutions acceptably match with each other for the middle region where $|x|$ is small. (d) Comparison with the Fresnel's solution (dashed line) in the log-scale Our solution matches extremely well with the Fresnel's solution. (e) The absolute difference between the computed intensity and that from the Fresnel approximation.

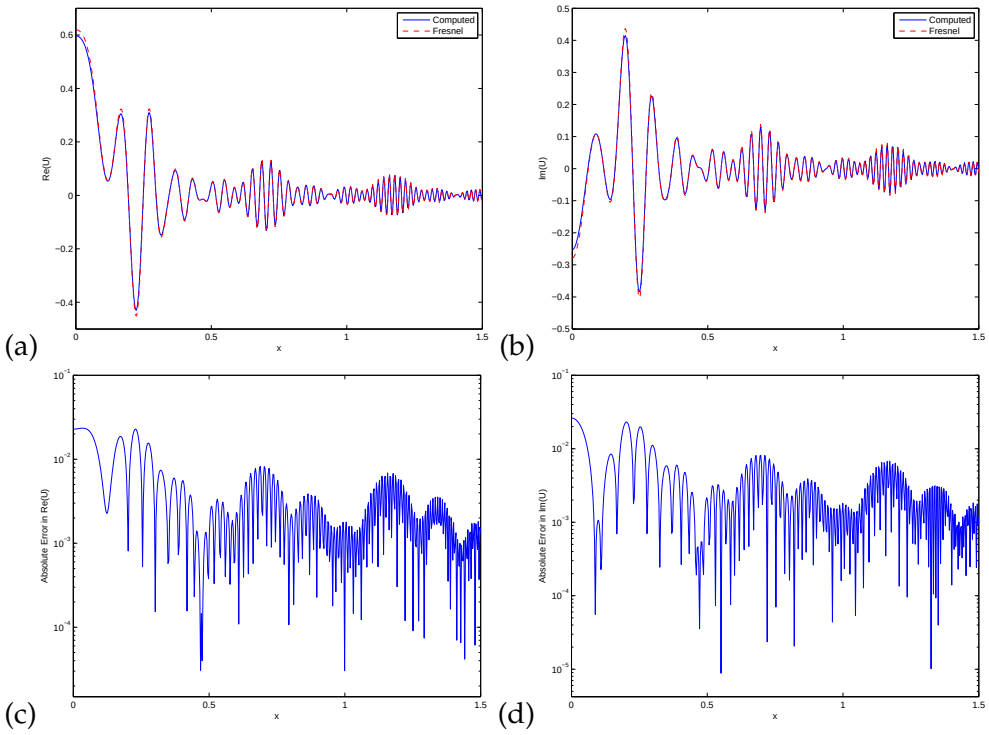

Figure 13: Double slit diffraction in homogeneous medium. The aperture is $b=0.1$ with an incident plane wave frequency $\omega=256\pi$. (a) The real part of the wavefield on $z=3$ and $0<x<1.5$. (b) The imaginary part of the wavefield on $z=3$ and $0<x<1.5$. (c) The absolute difference between the solution in (a) and that from the Fresnel approximation. (d) The absolute difference between the solution in (b) and that from the Fresnel approximation.

well with the Fresnel solution, as shown in (e). We have also compared our computed wavefield on $z=3$ with that from the Fresnel approximation in figure 13. These solutions match well as in the single diffraction case.

4.3 Gaussian Beam Diffraction in Lens-Like Medium

We study the diffraction of a Gaussian beam in a parabolic lens-like medium with the velocity given by

$$c(x,z)=\frac{1}{\sqrt{1-x^2}}. \tag{4.8}$$

This example has been widely studied in various articles [10, 4, 19, 3]. Considering an initial Gaussian wave profile given by

$$U(x,0)=\exp\left(-\frac{x^2}{2\sigma_0^2}\right), \tag{4.9}$$

with $\sigma_0=0.01$, we compute the solution to the Helmholtz equation with $\omega=64\pi$.

We initialize the level set $\Gamma(0)$ by $\{(x,\theta):|x|\leq 0.05,\theta=0\}$. Unlike in the previous example where the level set stays unmoved ($u=v=0$), the segment in this example will roughly rotate about the origin. Figure 14 shows the evolution of this segment. Our algorithm can give a nice quasi-uniform sampling of the evolving curve. In the phase space, caustic is defined as locations where the level set overturns, i.e. $\partial x/\partial\phi=0$ along the level set or the x-projection of the level set will change the number of arrivals. In the third and the seventh subplots in figure 14, we can see the overturn of the level set which clearly show the existence of caustics in the solution. Geometrical optics solution cannot correctly compute the results wavefield since this asymptotic approximation wrongly predicts that the amplitude will blow up at these caustic locations.

As discussed in those above cited references, the intensity of the wavefield can be well approximated by the following gaussian profile for small slit $|x|$ or small angle θ,

$$\begin{aligned} I(x,z) &= \frac{\sigma_0}{\sigma(z)}\exp\left(-\frac{x^2}{\sigma^2(z)}\right) \\ \sigma(z) &= \sigma_0\sqrt{1+\left[\left(\frac{1}{\omega\sigma_0^2}\right)^2-1\right]\sin^2(z)}. \end{aligned} \tag{4.10}$$

We have shown the computed wavefield in figure 15. The refocusing effect of this parabolic medium is clearly seen at around $z=\pi$ and $z=2\pi$. To compare these two solutions clearly, in figure 16 we plot the computed intensity with the exact values along $x=0$. These two solutions match well.

In figure 17, we have also plotted the ray tracing solution of the central beams. These Lagrangian beams are shotted from $z=0$ with takeoff angles equal zero and takeoff locations uniformly distributed along the x-direction. As seen clearly, all these rays collide

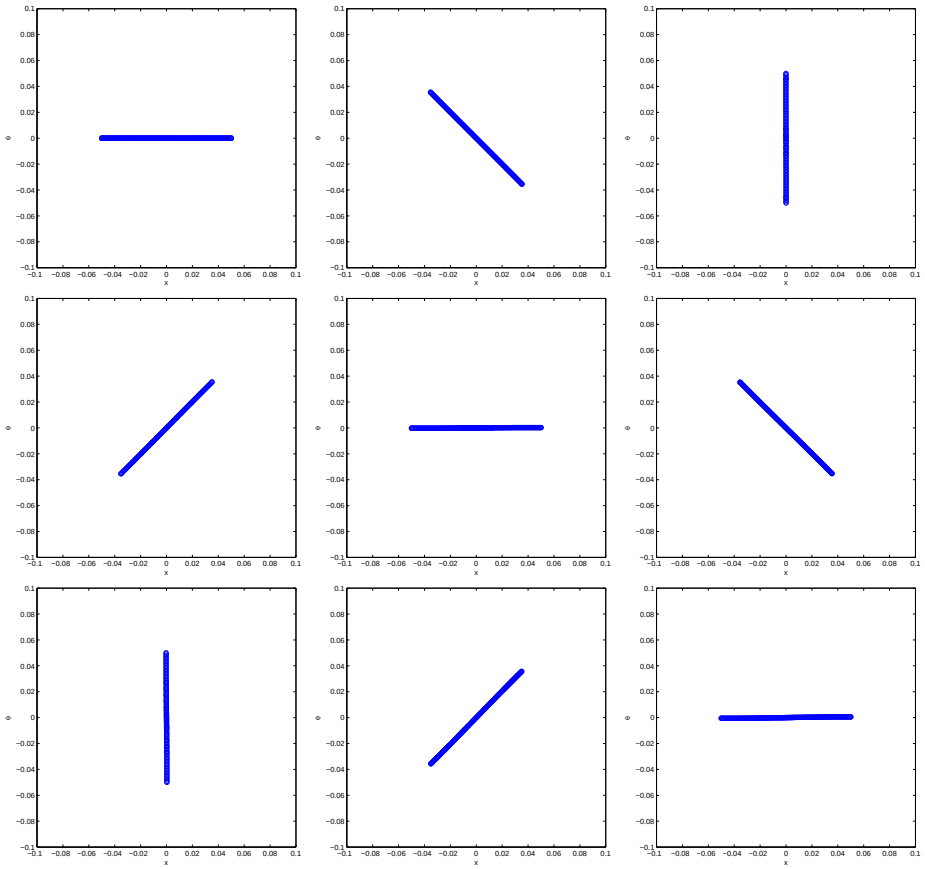

Figure 14: Diffraction of a Gaussian in a parabolic medium. We show the evolution of the open level curve in the $x-\theta$ phase space. Caustics are clearly observed at the third and the seventh subplot.

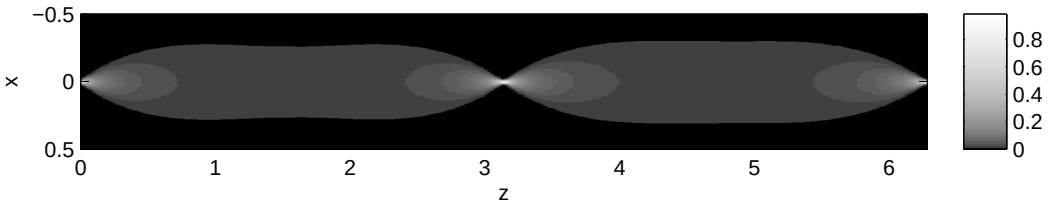

Figure 15: Diffraction of a Gaussian in a parabolic medium. The intensity $I(x,z)$.

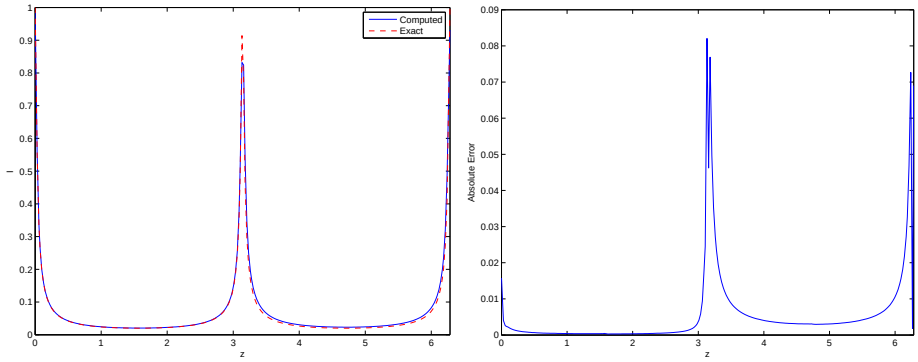

Figure 16: Diffraction of a Gaussian in a parabolic medium. (a) The intensity along $x=0$, $I(0,z)$. The refocusing effect is clearly seen at $z=\pi$ and 2π. (b) The absolute difference between the computed solution in (a) and that from the small-angle approximation.

and form caustics at $z=\pi/2$ and $z=3\pi/2$. Since we have all rays converging to a single point at these z-levels, the geometrical optics solution is not able to produce the right diffraction behavior in the wavefield. Our solution can capture the right behavior of the wave propagation even at caustics. In figure 18, we have shown the arrivaltimes at different z's. In the third and the seventh subplots, we have multiple arrivals that all rays almost converge to a single point.

4.4 Diffraction in Inhomogeneous Media

In this section, we will consider the diffraction pattern by a single slit in a sinusoidal medium with the velocity given by

$$c(x,z)=1+0.2\sin[3\pi(x+0.55)]\sin\left(\frac{\pi z}{2}\right). \tag{4.11}$$

The slit is placed at $z=0$ centered at $x=0$ with size $b=0.1$. The incident wave is a plane wave with frequency $\omega=64\pi$. We have shown a contour plot of the underlying velocity model in figure 19. This velocity model has been used widely to test the ability of a

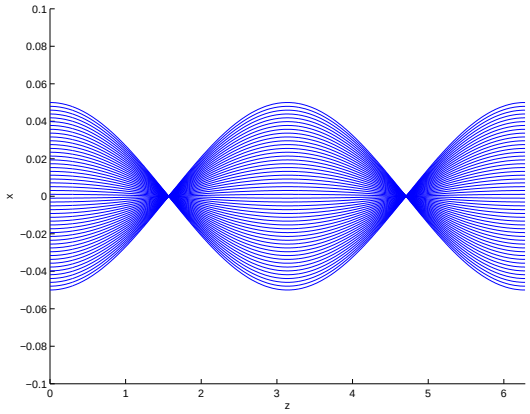

Figure 17: Diffraction of a Gaussian in a parabolic medium. The central beam location by ray tracing.

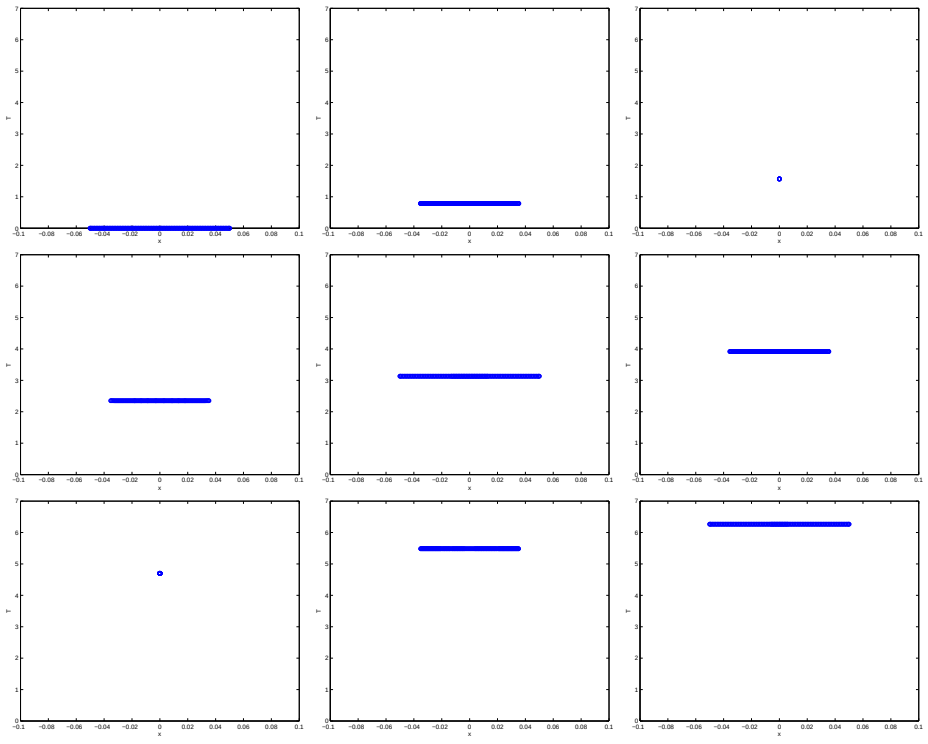

Figure 18: Diffraction of a Gaussian in a parabolic medium. We show arrivaltimes at various z's corresponding to that in figure 14. Multiple arrivals are observed at $(x,z) = (0,\pi/2)$ and $(0,3\pi/2)$ which corresponds to approximately the second and the seventh subplots.

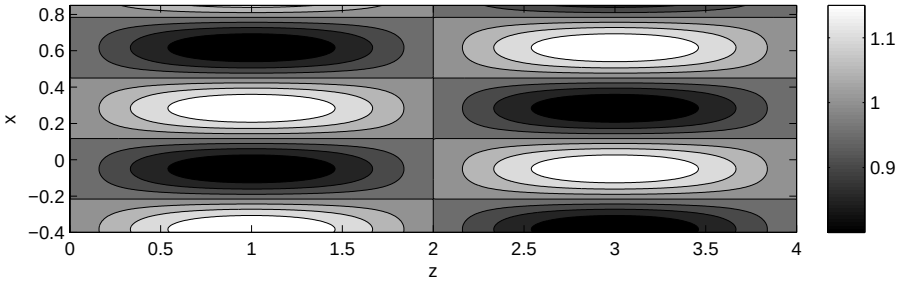

Figure 19: Diffraction of a plane wave in a sinusoidal medium. The contour plot of the underlying velocity model.

numerical method to obtain a nice representation of the multivalued arrivaltime solution [37, 38, 29, 30].

In figure 20, we plot the evolution of the open level curve in the $x-\theta$ phase space at different z's. At one end location with $x_0=-0.05$ and $\theta_0=0$, the velocities are $(u,v)|_{(x_0,\theta_0)}=(0,0)$. This implies that this end point is kept fixed in z. The other endpoint of the segment will move around according to the motion law, as shown in figure 21. Unlike the previous example, the open curve in this example is extensively stretched as it evolves in z. Usual Lagrangian type method will not be able to nicely sample this curve. As shown in figure 20, our numerical method can obtain a nice quasi-uniform sampling of this open level set while the end points are accurately tracked.

We shown in figure 22 the corresponding arrivaltimes of each arrival rays. As shown clearly in the last two subplots from both figure 20 and 22, we have two arrivals for z approximately greater than 3. For instance in the last subplot which corresponds to $z=4$, we have a caustic at around $x=0.77$. Same as in the previous example, the classical geometrical optics approximation fails to predict the amplitude at these locations. But the Gaussian beam approach can give finite amplitude solution as shown in the intensity plot of the wavefield in figure 23 (a). We show also the real and the imaginary parts of the wavefield in (b) and (c), respectively.

As an even more challenging example, we consider also the double slit diffraction pattern in this sinusoidal media. We use the same set-up as in Section 4.2 where we places two slits at $z=0$ which are separated by $a=0.1$ and with the width $b=0.05$. To resolve each slit using the same number of beams, we have doubled the number of mesh in each direction in the phase space. We have shown the evolution of the two segments in figure 24. The left segment is vigorously stretched under the velocity field but still our algorithm can nicely maintain a quasi-uniform sampling of the level curve and can accurately keep track of the end points in the evolution. Again, as in the single slit case, caustics are clearly observed in the last subplot. The overall wavefield, together with the real and the imaginary parts, are plotted in figure 25.

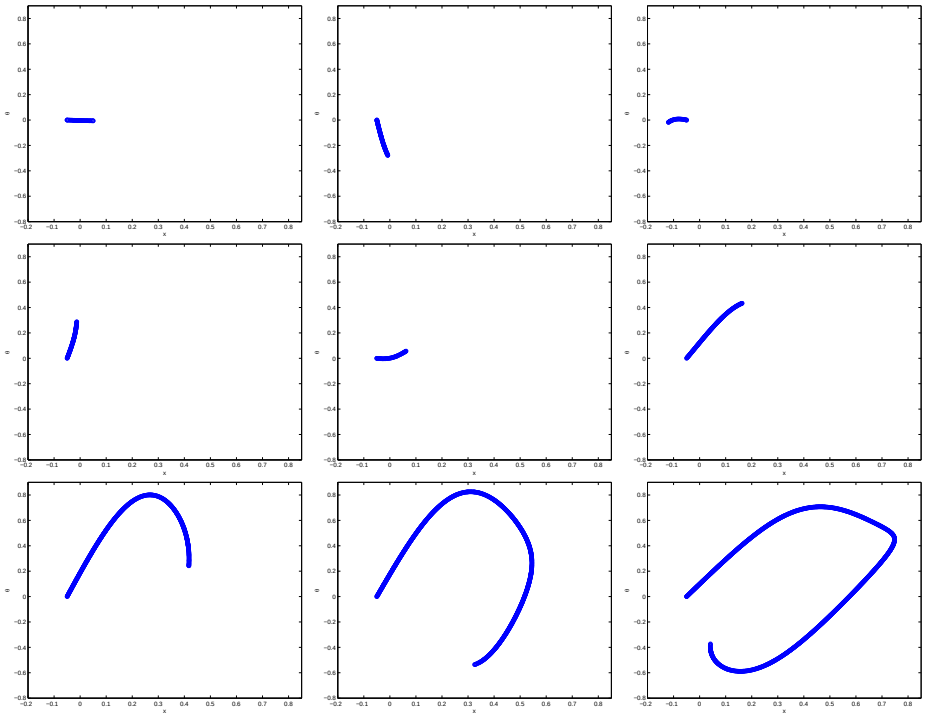

Figure 20: Diffraction of a plane wave in a sinusoidal medium. We show the evolution of the open level curve in the $x-\theta$ phase space at various z's. The multiple arrivals are clearly seen at the last two subplots.

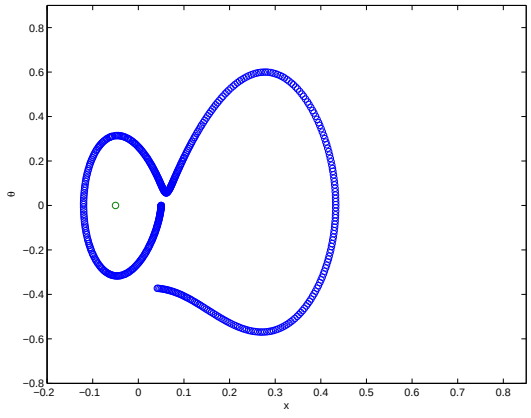

Figure 21: Diffraction of a plane wave in a sinusoidal medium. The end points of the open level set for all z. Since u and v are both zero at $(x,\theta)=(-0.05,0)$, one of the end-point is kept fixed.

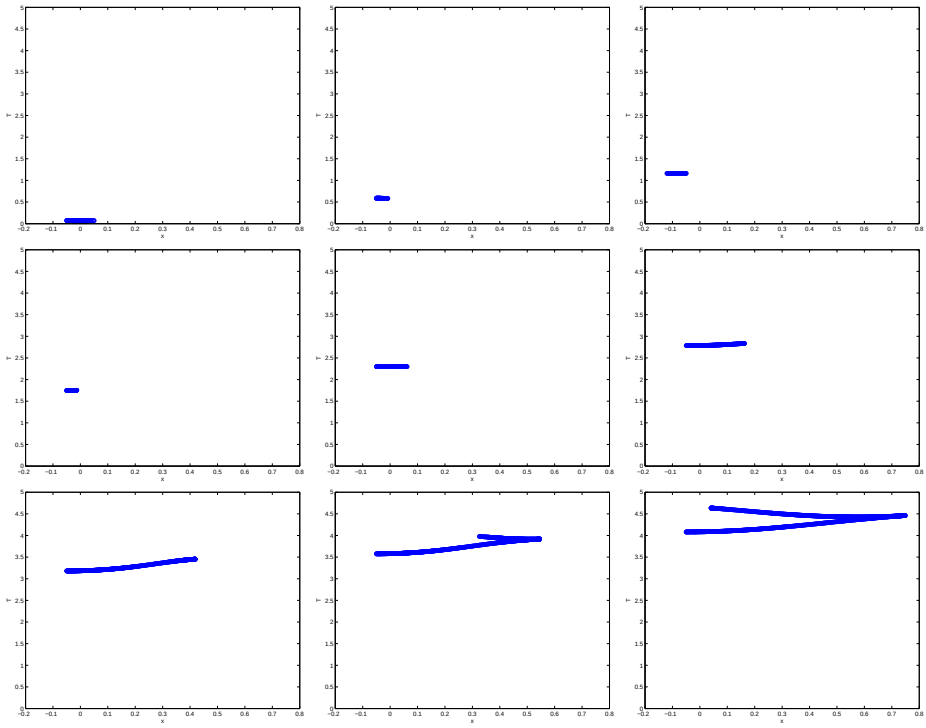

Figure 22: Diffraction of a plane wave in a sinusoidal medium. We show the arrivaltimes at various z's. Two arrivals are clearly seen at the last two subplots.

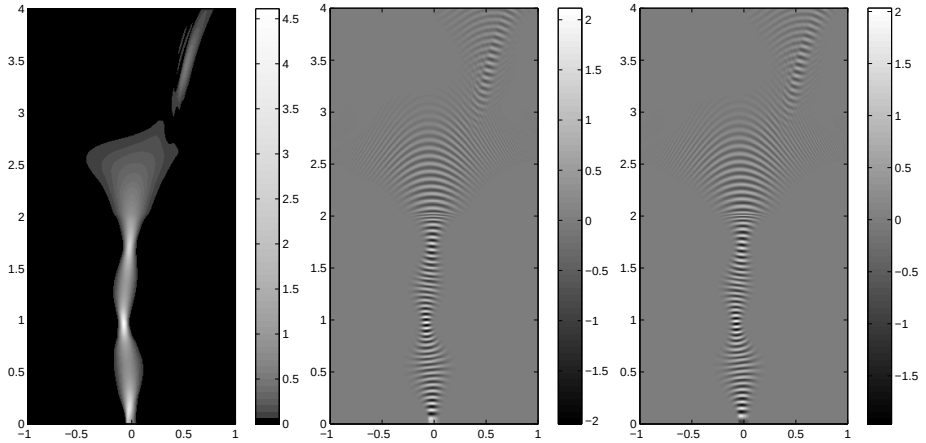

Figure 23: Diffraction of a plane wave in a sinusoidal medium. (a) The intensity of the wavefield. (b) The real part of the wavefield. (c) The imaginary part of the wavefield.

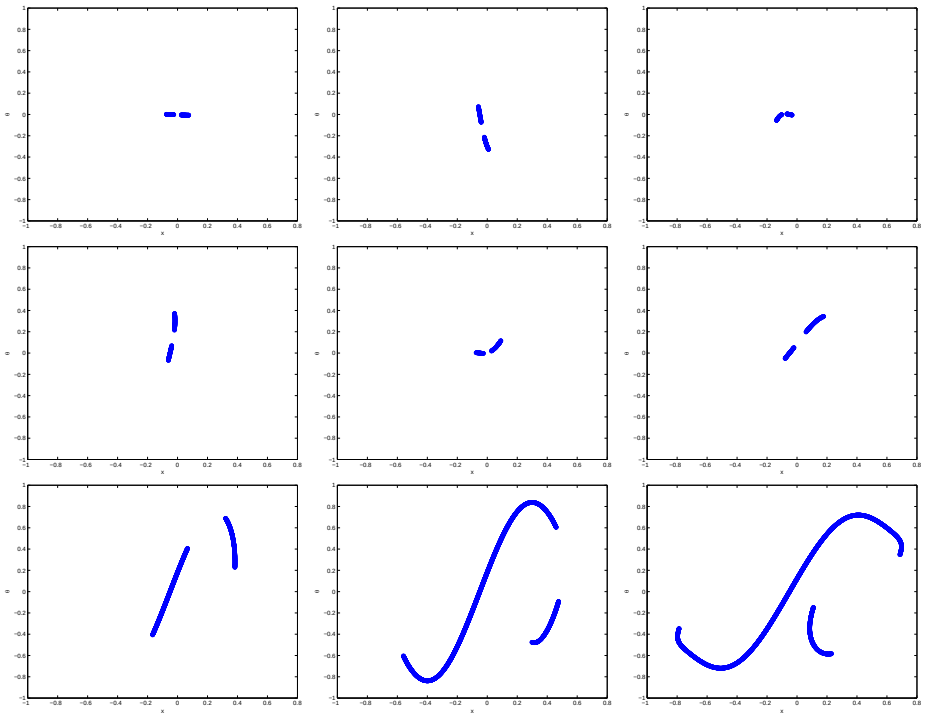

Figure 24: Diffraction of a plane wave in a sinusoidal medium. We show the evolution of the open level curve in the $x-\theta$ phase space at various z's. The multiple arrivals are clearly seen at the last two subplots.

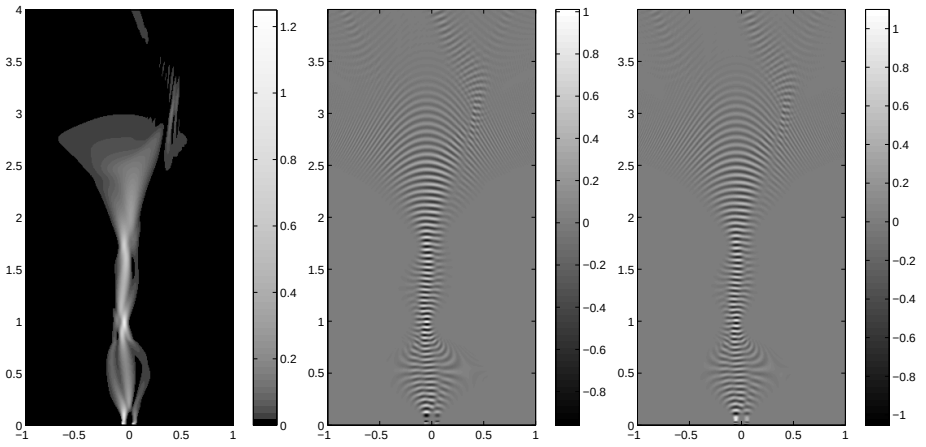

Figure 25: Diffraction of a plane wave in a sinusoidal medium. (a) The intensity of the wavefield. (b) The real part of the wavefield. (c) The imaginary part of the wavefield.

Acknowledgements

The work of Leung was supported in part by the RGC under Grant DAG09/10.SC02. The work of Zhao was supported in part by the ONR grant N00014-02-1-0090 and also in part by the NSF grant DMS0811254.

References

[1] V.M. Babich and V.S. Buldyrev. *Asymptotic Methods in Short Wave Diffraction Problems (in Russian)*. Nauka, Moscow, 1972.

[2] S. Basu, D.P. Mukherjee, and S.T. Acton. Implicit evolution of open ended curves. *IEEE International Conference on Image Processing*, 1:261–264, 2007.

[3] P. Berczynski, Y.A. Kravtsov, and G. Zeglinski. Gaussian beam diffraction in inhomogeneous and nonlinear media: Analytical and numerical solutions by complex geometrical optics. *Central European Journal of Physics*, 6:603–611, 2008.

[4] M. Bornatici and O. Maj. Wave beam propagation in a weakly inhomogeneous isotropic medium: Paraxial approximation and beyond. *Plasma Phys. Control. Fusion*, 45:707–719, 2003.

[5] M.D. Buhmann. *Radial Basis Functions*. Cambridge University Press, 2003.

[6] P. Burchard, L.-T. Cheng, B. Merriman, and S. Osher. Motion of curves in three spatial dimensions using a level set approach. *J. Comput. Phys.*, 170(2):720–741, 2001.

[7] V. Cerveny, M. M. Popov, and I. Psencik. Computation of wave fieds in inhomogeneous media - gaussian beam approach. *Geophys. J. R. astr. Soc.*, 70:109–128, 1982.

[8] L.-T. Cheng, P. Burchard, B. Merriman, and S. Osher. Motion of curves constrained on surfaces using a level-set approach. *J. Comput. Phys.*, 175:604–644, 2002.

[9] S. Choudhary and L.B. Felsen. Asymptotic theory for inhomogeneous waves. *IEEE Transactions on Antennas and Propagation*, AP-21:827–842, 1973.

[10] S. Choudhary and L.B. Felsen. Analysis of gaussian beam propagation and diffraction by inhomogeneous wave tracking. *Proceedings of the IEEE*, 62:1530–1541, 1974.

[11] R.A. Egorchenkov and Y.A. Kravtsov. Complex ray-tracing algorithms with application to optical problems. *J. Opt. Soc. Am. A.*, 18:650–656, 2001.

[12] B. Fornberg and N. Flyer. The gibbs phenomenon for radial basis functions. In A. Jerri, editor, *The Gibbs Phenomenon in Various Representations and Applications*. Potsdam, 2007.

[13] G.R. Fowles. *Introduction to Modern Optics*. Dover, 1989.

[14] J. Gomes and O. Faugeras. Using the vector distance functions to evolve manifolds of arbitrary codimension. *Lecture Notes In Computer Science*, 2106:1–13, 2001.

[15] N. R. Hill. Gaussian beam migration. *Geophysics*, 55:1416–1428, 1990.

[16] L. Hormander. On the existence and the regularity of solutions of linear pseudo-differential equations. *L'Enseignement Mathematique*, 17:99–163, 1971.

[17] J.B. Keller. Geometrical theory of diffraction. *Journal of the Optical Society of America*, 52:116–130, 1962.

[18] R.G. Kouyoumjian. *Self-Focusing: Past and Present*, chapter 6 The Geometrical Theory of Diffraction and its Application, pages 165–215. Springer, 2006.

[19] Y.A. Kravtsov and P. Berczyski. Gaussian beams in inhomogeneous media: A review. *Stud. Geophys. Geod.*, 51:1–36, 2007.

[20] S. Leung and J. Qian. Eulerian gaussian beams for schrodinger equations in the semi-classical regime. *J. Comput. Phys.*, 228:2951–2977, 2009.

[21] S. Leung, J. Qian, and R. Burridge. Eulerian gaussian beams for high frequency wave propagation. *Geophysics*, 72:SM61–SM76, 2007.

[22] S. Leung, J. Qian, and S. Osher. A level set method for three-dimensional paraxial geometrical optics with multiple sources. *Commun. Math. Sci.*, 2(4):643–672, 2004.

[23] S. Leung and H.K. Zhao. A grid-based particle method for evolution of open curves and surfaces. *J. Comput. Phys.*, 228:7706–7728, 2009.

[24] S. Leung and H.K. Zhao. A grid based particle method for moving interface problems. *J. Comput. Phys.*, 228:2993–3024, 2009.

[25] M. Motamed and O. Runborg. A fast phase space method for computing creeping rays. *J. Comput. Phys.*, 219:276–295, 2006.

[26] Y.I. Orlov and S.K. Tropkin. Penumbral diffraction fields in inhomogeneous media. *Radiophysics and Quantum Electronics*, 24:233–240, 1981.

[27] S. Osher and R. P. Fedkiw. *Level Set Methods and Dynamic Implicit Surfaces*. Springer-Verlag, New York, 2003.

[28] S. J. Osher and J. A. Sethian. Fronts propagating with curvature dependent speed: algorithms based on Hamilton-Jacobi formulations. *J. Comput. Phys.*, 79:12–49, 1988.

[29] J. Qian and S. Leung. A level set based eulerian method for paraxial multivalued traveltimes. *J. Comput. Phys.*, 197:711–736, 2004.

[30] J. Qian and S. Leung. A local level set method for paraxial multivalued geometric optics. *SIAM J. Sci. Comput.*, 28:206–223, 2006.

[31] J. Ralston. Gaussian beams and the propagation of singularities. *Studies in partial differential equations*, 23:206–248, 1983.

[32] B.D. Seckler and J.B. Keller. Asymptotic theory of diffraction in inhomogeneous media. *The Journal of the Acoustical Society of America*, 31:206–216, 1959.

[33] B.D. Seckler and J.B. Keller. Geometrical theory of diffraction in inhomogeneous media. *The Journal of the Acoustical Society of America*, 31:192–205, 1959.

[34] C. W. Shu and S. J. Osher. Efficient implementation of essentially non-oscillatory shock capturing schemes. *J. Comput. Phys.*, 77:439–471, 1988.

[35] P. Smereka. Spiral crystal growth. *Physica D*, 138:282–301, 2000.

[36] J.E. Solem and A. Heyden. Reconstructing open surfaces from image data. *International Journal of Computer Vision*, 69:267–275, 2006.

[37] W. W. Symes. A slowness matching finite difference method for traveltimes beyond transmission caustics. In *68th Ann. Internat. Mtg., Soc. Expl. Geophys., Expanded Abstracts*, pages 1945–1948. Soc. Expl. Geophys., 1998.

[38] W. W. Symes and J. Qian. A slowness matching Eulerian method for multivalued solutions of eikonal equations. *J. Sci. Comp.*, 19:501–526, 2003.

[39] N. Tanushev. Superpositions and higher order gaussian beams. *Commun. Math. Sci.*, 6:449–475, 2008.

[40] N. Tanushev, J. Qian, and J. Ralston. Mountain waves and gaussian beams. *SIAM J. Multi. Model. & Simul.*, 6:688–709, 2007.

[41] H.-K. Zhao, T. Chan, B. Merriman, and S. J. Osher. A variational level set approach for multiphase motion. *J. Comput. Phys.*, 127:179–195, 1996.